1991

Theoretical studies of amorphous silicon and hydrogenated amorphous silicon with molecular dynamics simulations

Inhee Kwon
Iowa State University

INFORMATION TO USERS

This manuscript has been reproduced from the microfilm master. UMI films the text directly from the original or copy submitted. Thus, some thesis and dissertation copies are in typewriter face, while others may be from any type of computer printer.

The quality of this reproduction is dependent upon the quality of the copy submitted. Broken or indistinct print, colored or poor quality illustrations and photographs, print bleedthrough, substandard margins, and improper alignment can adversely affect reproduction.

In the unlikely event that the author did not send UMI a complete manuscript and there are missing pages, these will be noted. Also, if unauthorized copyright material had to be removed, a note will indicate the deletion.

Oversize materials (e.g., maps, drawings, charts) are reproduced by sectioning the original, beginning at the upper left-hand corner and continuing from left to right in equal sections with small overlaps. Each original is also photographed in one exposure and is included in reduced form at the back of the book.

Photographs included in the original manuscript have been reproduced xerographically in this copy. Higher quality 6" x 9" black and white photographic prints are available for any photographs or illustrations appearing in this copy for an additional charge. Contact UMI directly to order.

U·M·I

University Microfilms International
A Bell & Howell Information Company
300 North Zeeb Road, Ann Arbor, MI 48106-1346 USA
313/761-4700 800/521-0600

Order Number 9212155

Theoretical studies of amorphous silicon and hydrogenated amorphous silicon with molecular dynamics simulations

Kwon, Inhee, Ph.D.

Iowa State University, 1991

U·M·I
300 N. Zeeb Rd.
Ann Arbor, MI 48106

Theoretical studies of amorphous silicon and hydrogenated amorphous silicon with molecular dynamics simulations

by

Inhee Kwon

A Dissertation Submitted to the

Graduate Faculty in Partial Fulfillment of the

Requirements for the Degree of

DOCTOR OF PHILOSOPHY

Department: Physics and Astronomy
Major: Solid State Physics

Approved:

Signature was redacted for privacy.

In Charge of Major Work

Signature was redacted for privacy.

For the Major Department

Signature was redacted for privacy.

For the Graduate College

Iowa State University
Ames, Iowa
1991

TABLE OF CONTENTS

LIST OF TABLES

LIST OF FIGURES

ACKNOWLEDGEMENTS

I wish to express my deep appreciation to my advisor Professor Costas M. Soukoulis for his guidance and support for this study. I would like to express my special gratitude to Dr. Rana Biswas for his suggestions, stimulating discussions, and support all the way from the beginning to the end of this work.

I would also like to thank my family, especially my husband Jin Hyung Cho, for their constant encouragement and support throughout the study.

This work was performed at Ames Laboratory under contract no. W-7405-eng-82 with the U. S. Department of Energy. The United States government has assigned the DOE Report number IS-T 1587 to this dissertation. I acknowledge support from the Electric Power Research Institute under the amorphous thin film solar cell program. I also acknowledge an National Science Foundation grant of Supercomputer time at the National Center for Supercomputer Applications, Champaign, Illinois.

CHAPTER 1. INTRODUCTION

Amorphous semiconductors are lack of long-range translational order (periodicity), characteristic of a crystal [1, 2]. However, amorphous semiconductors are not completely disordered on the atomic scale. Local chemistry provides almost rigorous bond-length, and to a lesser extent, bond-angle constraints on the nearest-neighbor environment. Unlike amorphous metals, amorphous semiconductors do not consist of close-packed atoms, but rather they contain covalently bonded atoms arranged in an open network with spatial correlations extending up to third or fourth nearest neighbors. The short-range order is directly responsible for observable semiconductor properties such as optical absorption edges and activated electrical conductivities.

The absence of long-range order, or periodicity, characteristic of amorphous materials is most clearly evidenced in a diffraction experiment, for example using X-rays, where instead of the sharp Bragg spots or rings produced by single crystal or polycrystalline samples respectively, broad diffuse haloes are observed. However, it is sometimes extremely difficult to ascertain by diffraction means alone whether a given material is truly amorphous or is simply microcrystalline or even nanocrystalline (i.e., consisting of crystallites whose size is of the order of a few nanometers); in both cases broad haloes can be observed. Polycrystalline semiconductors are composed of grains with each grain containing a periodic array of atoms surrounded by

a layer of interconnective or boundary atoms. The distinction between amorphous and microcrystalline samples can be made by a calorimetric test [3]. The crystallization of a truly amorphous material occurs by means of 'nucleation and growth' of the crystallites, whereas an already microcrystalline material will simply experience overall grain growth of the crystallites; these two processes have fundamentally different kinetics, in principle enabling the two types of materials to be distinguished.

Among amorphous semiconductors, chalcogenide glasses are prepared from a semiconductor melt by rapid cooling (quenching) to temperatures below the glass transition temperature. For silicon and other group IV materials, quenching from the melt, that is metallic and has a different short-range order than the desired semiconductors, generally cannot be done rapidly enough to freeze in an amorphous atomic arrangement. Polycrystalline is the more common result. Amorphous semiconductors that cannot be prepared directly from the melt are usually fabricated in the form of thin films by atomic deposition procedures such as evaporation, sputtering, chemical vapor deposition, plasma decomposition of gases, or electroplating. Sometimes ion bombardment of crystals is used to leave an amorphous layer in the collision trail of the ions.

Amorphous materials have many advantages over their crystalline counterparts where applications are concerned. In general, amorphous solids are relatively easy to prepare: large-area, homogeneous amorphous thin films can be prepared, especially the hydrogenated amorphous silicon (a-Si:H) films for solar-cell or thin-film transistor applications. Amorphous materials have a further, distinct advantage over their crystalline counterparts in that homogeneous amorphous phases can often be formed in mixed-component systems over rather wide ranges of composition, not necessarily

restricted to stoichiometric values. For this reason, physical properties of such amorphous materials can often be varied continuously simply by varying the composition. Thus, the intrinsic optical properties, namely the optical band gap, of amorphous semiconductors can be varied systematically by changing the composition of an alloy system, e.g. a-$Si_{1-x}C_x$:H.

Compared to extensive materials studies of amorphous materials, relatively few aspects are clearly understood in the fundamental physics of such systems. For example, it is commonly believed that the origin of electron spin resonance (ESR) signal in amorphous silicon is an undercoordinated defect (dangling bond). However, there is a recent argument [4] to suggest that the paramagnetic defect center may be an overcoordinated defect (floating bond). Both interstitials and vacancies exist in crystals and it is argued the same should be true in a-Si.

The performance of amorphous silicon-based solar cells is limited by light-induced degradation (the Staebler-Wronski effect) [5]. It has also been found that high-energy particle irradiation, quenching at high temperature, and current injection can affect the instability of amorphous silicon. All of these effects are reversible by annealing to a sufficiently high temperature, and all are believed to be caused by the same degradation mechanism [6]. Several models [7, 8, 9, 10, 11, 12, 13, 14, 15, 16] have been proposed, both phenomenological and microscopic, but no model has been estabilished to explain all experimental observations. Even the answer to the question, whether the degradation is inherent and intrinsic to amorphous silicon, is not clear yet.

Knowledge of the structural arrangement of atoms of a solid substance is an essential prerequisite to a detailed understanding of other physical or chemical proper-

ties. A variety of experimental techniques can give information about the microscopic structure of amorphous solids. In most cases, and for diffraction experiments in particular, this information is limited almost entirely to the first two coordination shells in the case of covalent materials; i.e., the bond lengths and angles of nearest-neighbor atoms comprising the basic structural unit can be determined, but the relative disposition of such units cannot be ascertained with certainty. Matters are complicated considerably for multicomponent materials for which a single diffraction experiment does not identify the origin of any peak in the radial distribution in terms of specific atomic pair correlations.

Structural modeling can be a valuable aid to determining the structure of amorphous solids. A model built using knowledge about local order of the system, and whose computed scattering properties (e.g. structure factor, radial distribution function, etc.) fit well those derived from experiment, can give considerable additional insight into the structure, which otherwise cannot be obtained. The importance of structural modeling lies in the fact that a detailed understanding of the structure may thereby be gained.

Many structural models of amorphous materials have been physical models, either of the 'ball-and-stick' type [17, 18] (for continuous random networks and other models of covalent materials) or random packings of spheres [19] (for metallic solids) because visualization of the model is most important. Nevertheless, for convenience many models have been constructed using a computer. Computer methods can be easily modified (e.g. due to strain-energy relaxation) or transformed. Using Monte Carlo simulations, models are constructed by the random positioning of atoms starting from either a crystalline [20] or another amorphous structure. Computer tech-

niques also figure prominently in molecular dynamics simulations [21, 22, 23, 24]. Molecular dynamics, as its name implies, involves the study of the time evolution of the classical motion of a collection of atoms (or molecules), interacting by means of a given interatomic potential, as a function of the change in temperature (or some other thermodynamic variable) of the system. The advantages of the molecular dynamics approach include a detailed knowledge of the time evolution of the atomic positions and momenta, and the ability to impose instantaneous changes of thermodynamic variables, such as pressure and temperature, on the system and to monitor the concomitant changes, if any. The disadvantage of the method is that the time scales in such computer simulations are several orders less than experimental time scales. The small time step is needed in the simulation and in most cases, total simulation time can seldom exceed $\simeq 10^{-10}$ s, as a result of computer economics. Also, there are appreciable difficulties in developing interatomic potentials, especially for covalent-bonding systems.

In this dissertation, structural modeling of amorphous silicon and hydrogenated amorphous silicon has been studied with molecular dynamics simulations. A new Si-H interatomic potential has been developed for Si-H interactions. Based on these realistic atomic models, stabilities of the materials have been studied with the aim of understanding microscopic mechanisms underlying light-induced degradation of hydrogenated amorphous silicon.

It should be noted that a structural model, of whatever type, is always an idealization of the true structure of an amorphous solid. Unlike a crystal, there is no unique structure of an amorphous material. Furthermore, it is difficult for structural models to take account of the growth processes and the resulting morphologies

which occur in real amorphous systems. The finite size of the models also needs to be considered carefully. Despite several disadvantages of the molecular dynamics simulations, it can be shown that theoretical simulations account well for many experimental observations.

CHAPTER 2. STRUCTURAL MODELING OF AMORPHOUS SILICON

Amorphous silicon films are commonly deposited with sputtering or glow-discharge methods that involve room-temperature or somewhat warmer (200° - 250° C) substrates resulting in limited surface diffusion of the deposited species leading to amorphous film growth. Recently, Takagi and co-workers [25] have demonstrated that the ionized-cluster-beam (ICB) technique is a viable deposition technique for growing Si films. In the ICB technique, atomic clusters are generated by an adiabatic expansion of condensed vapor atoms through a nozzle into a high vacuum region. The clusters are positively ionized by an electron beam, and accelerated toward the deposition surface. The ICB process is characterized by the charged deposition species as well as a control over the incident kinetic energy of the cluster - which is an additional degree of freedom not present in the molecular beam case.

Many aspects of the ICB growth techniques are not well understood, and with a view toward understanding these, we perform a simulation of a-Si film growth with cluster-beam deposition. We and Biswas et al. [26] have characterized the spreading of clusters and surface diffusion of the deposited species to the deposition conditions, i.e., incident cluster velocity, cluster temperature, substrate temperature, and cluster size. Based on these results, we perform simulations of amorphous film growth by

choosing the deposition conditions of low surface diffusion. Conversely, we have also grown epitaxial crystalline silicon films by choosing conditions of high surface diffusion.

There has been much recent activity in the development of a-Si models with molecular dynamics [21, 22, 23, 27]. In all cases, quenching of a melt of bulk Si with periodic boundary conditions was used to generate the amorphous phase. These molecular dynamics studies have utilized the Stillinger-Weber [28] and the Tersoff model [29], as well as the Biswas-Hamann model [30] for the interatomic Si potentials. The structural models exhibit root-mean-square (rms) bond-angle distortions between 10° and 14°, and rms bond-length variations of about 2 %. The vibrational densities of the states compared very well with experiment for both the transverse-acoustic (TA) and transverse-optic (TO) peaks. A new feature of these models is the presence of coordination defects consisting primarily of three- and five-coordinated Si atoms. In fact, the five-coordinated Si atom or floating bond was proposed by Pantelides [4] to be a novel intrinsic defect in a-Si and a-Si:H that could account for various ESR and H-diffusion measurements. In the various molecular dynamics generated a-Si models, there were either five-coordinated atoms as the only or majority defects [21, 23, 27] or there were both three- and five-coordinated sites in comparable numbers [22].

A drawback of the a-Si models discussed to date is that the melt-quenched process by which they are generated is in many ways different from the experimental growth process of deposition on a cold substrate by which all a-Si films are commonly grown. In fact, Phillips [31] has observed that the kinetics of the growth from a vapor phase should not favor overcoordination defects, but favor undercoordination defects

instead. In this chapter, we systematically compare the properties of the deposited a-Si models with the bulk melt-quenched models and identify important consequences both for the floating-bond hypothesis and for evaluating the previous a-Si models themselves.

A major difficulty exists in comparing results of molecular dynamics simulations with experiments. Owing to limitations in computer time and the small time step that is used, the molecular dynamics simulations are typically performed over real-time scales of a few nanoseconds, which are several orders of magnitude smaller than time scales in experiments. Hence, the simulations cannot address long-time dynamical properties such as long-range diffusion of atoms. On the other hand, molecular dynamics with realistic interatomic interactions well describe many aspects of shorter range and smaller time relaxations, which as we will see is crucial in describing amorphous growth.

Computational Method

Although a number of classical models [28, 29] for interatomic Si interactions may be equally suitable for simulations of Si film-growth processes, we have used the Biswas-Hamann model [30] of separable two- and three-body interatomic potentials. In this model, the structural energy is defined by the following form:

$$E = \frac{1}{2}\sum_{1,2}{}' V_2(1,2) + \sum_{1,2,3}{}' V_3(1,2,3)\,, \tag{2.1}$$

where primes indicate that all summation indices are distinct. The two-body potential is

$$V_2(r) = [A_1 \exp(-\lambda_1 r^2) + A_2 \exp(-\lambda_2 r^2)] f_c(r)\,, \tag{2.2}$$

where $f_c(r)$ is the cutoff function,

$$f_c(r) = [1 + \exp(\frac{r - r_c}{\mu})]^{-1}. \tag{2.3}$$

The three-body potential is

$$V_3(r_{12}, r_{13}, \theta) = B\psi(r_{12})\psi(r_{13})(\cos\theta + \frac{1}{3})^2 f_c(r_{12}) f_c(r_{13}), \tag{2.4}$$

where $\psi(r)$ is the radial function,

$$\psi(r) = \exp(-\alpha r^2). \tag{2.5}$$

This model was originally developed by fitting to first-principles total-energy calculations for energies of bulk, surface, and defect Si configurations [32]. A strengthening of the three-body potential by a factor of 2.50 was found to be necessary for describing a-Si in the previous work [22].

The estimated melting temperature of the original Biswas-Hamann potential is between 0.24 and 0.26 eV, which is somewhat higher than experimental melting temperature $k_B T_m$ of 0.147 eV. One of the reasons for using this potential is that a number of melt-quenched a-Si models were previously generated with this model. These melt-quenching simulations consisted of equilibrating a liquid Si configuration which was then cooled to generate an amorphous structure. Therefore, deposition simulations with the same model can give a direct comparison of the difference between these two simulation methods of preparing a-Si. Also, Biswas et al. [26] have already studied the dependence of the surface diffusivity to the deposition conditions with this potential, and these results can be directly utilized in this work.

The simulation system (Figure 2.1) consisted of four movable Si(111) double layers above two immobile Si(111) double layers that modeled the underlying crystal.

A rectangular cell, with dimensions 20.25 and 21.06 Å consisting of 60 Si atoms per Si(111) double layer, with periodic boundary conditions in the x and y directions was used for the amorphous growth simulations. An in-plane lattice spacing of 4.05 Å was used for the Si(111) substrate corresponding to the equilibrium value for this Si interatomic potential model. Clusters with center-of-mass velocity v_z toward the substrate were introduced into the system from a large enough height so that they were outside the range of interaction of substrate atoms or previously deposited cluster atoms.

In the molecular dynamics calculations, Newton's equations of motion have been integrated in time, with the Gear fifth-order predictor-corrector algorithm [33], for a collection of substrate and deposited Si atoms. The first 5 derivatives of the position are calculated at time $t + \Delta t$ by Taylor-series expansions in terms of the same 5 derivatives at time t;

$$\frac{d^n}{dt^n}\vec{r}^{(P)}(t+\Delta t) = \sum_{k=0}^{5-n} \frac{(\Delta t)^k}{k!}\frac{d^k}{dt^k}\vec{r}(t), \quad \forall n = 0, 1, \ldots, 5\,. \tag{2.6}$$

The superscript (P) on the position vector indicates that this is the new *predicted* position. This new position is now corrected in the following way: The forces are reevaluated at the new predicted coordinates and compared with the forces determined from the new predicted accelerations. From the difference between these two estimates of the forces, a force correction parameter is computed, viz.,

$$\Delta\vec{F} = \frac{1}{2}(\Delta t)^2[\frac{1}{M}\vec{F}(t+\Delta t) - \frac{d^2}{dt^2}\vec{r}^{(P)}(t+\Delta t)]\,, \tag{2.7}$$

where M, the single-particle mass, is the Si atomic mass in this simulation. The predicted parameters computed in Eq. (2.6) are now corrected with the Gear coefficients

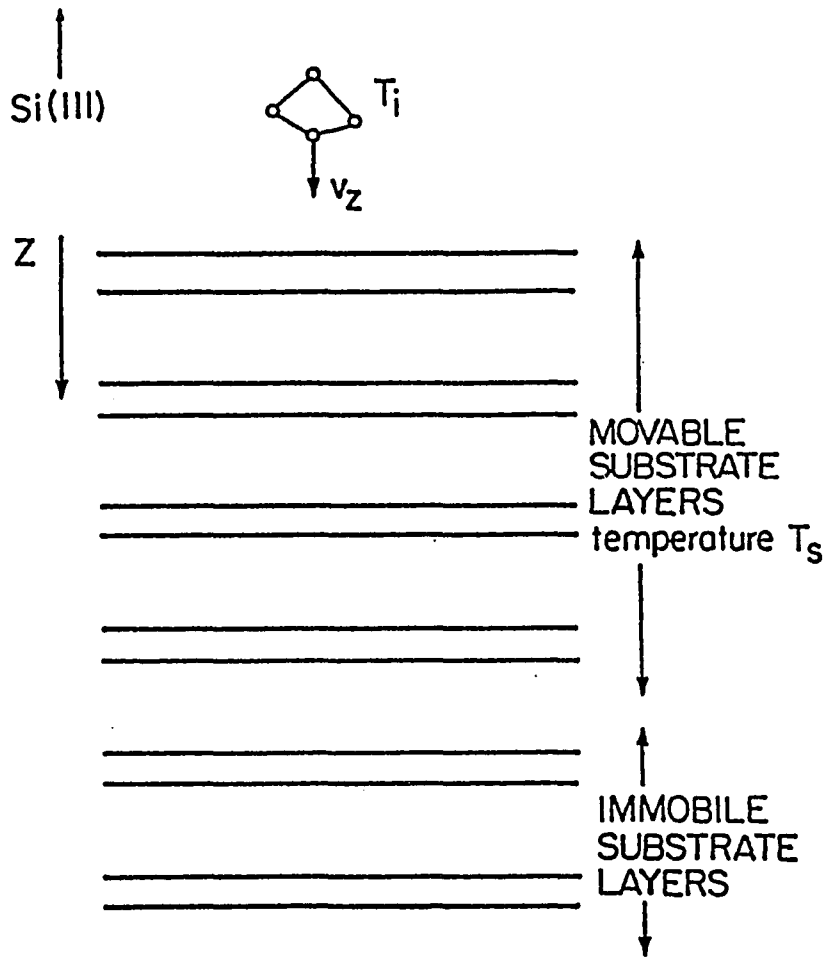

Figure 2.1: Schematic diagram of the system used for the simulations. The substrate consists of four Si(111) double layers, below which are two fixed Si(111) double layers. Clusters with internal temperature T_i are incident with center-of-mass velocity v_z on the substrate

G_i as follows:

$$\frac{d^n}{dt^n}\vec{r}^{(C)}(t+\Delta t) = \frac{d^n}{dt^n}\vec{r}^{(P)}(t+\Delta t) + \frac{n!}{(\Delta t)^n} G_n \Delta\vec{F}, \ \forall n = 0,\ldots,5, \qquad (2.8)$$

where $G_0 = \frac{1}{16}$, $G_1 = \frac{251}{360}$, $G_2 = 1$, $G_3 = \frac{11}{18}$, $G_4 = \frac{1}{6}$, and $G_5 = \frac{1}{60}$. The superscript (C) denotes the *corrected* positions. These new corrected values are now taken as the current position, velocity, acceleration, etc., and all analyses at this time step are performed using these values. This entire procedure is then iterated for the duration of the simulation. The time step (Δt) used in this work is 0.0037 ps, which is an appropriately small fraction of the silicon-optical-phonon period of 0.0638 ps.

In the entire simulation process, the temperature of the substrate is maintained at a constant temperature T_s. In any thin film growth experiment, heat energy is added to the surface by the deposited species. In our simulations, we model this thermal-conduction process by monitoring the average temperature of movable substrate layers every ten time steps. If this temperature exceeds the desired temperature T_s, the velocities of the atoms in the movable layers are rescaled to maintain a constant T_s. Therefore, the substrate layer acts as a heat reservoir that absorbs heat through collisions with the deposited species. We can increase this energy transfer rate by extending the velocity rescaling to include some of the deposited atoms also, and this has been used in the amorphous growth.

Sensitivity of Surface Diffusion to Deposition Conditions

As recognized in previous studies [26, 34], an important requirement in growing epitaxial films from cluster deposition is that each impinging cluster should dissociate and spread uniformly on the substrate. Alternatively, if the spreading of the cluster

is small, amorphous layer growth is expected. It has been also demonstrated that cluster-beam growth simulations are feasible and require substantially less computer time than simulations with single-atom deposition [26]. The reason is that the adsorbed cluster atoms equilibrate with the substrate more rapidly, allowing the next cluster to be deposited sooner than with single atom deposition. This is because the clusters initially have a considerable amount of binding energy. On adsorption, there is a smaller increase in the binding energy per atom for the cluster than for the single atom case, and consequently less kinetic energy gained or less heating of the cluster than the single atom.

We explore the parameter space of deposition parameters to define parameter ranges suitable for amorphous growth. It would be computationally unfeasible to simulate fully the growth of a thick film under different deposition conditions, and then differentiate between deposition parameters by examining the structure of the films. Instead, we adopt the much simpler procedure of studying the dynamics of deposition of a single cluster under different deposition conditions, to gain insight into the important parameters for the growth process.

To accomplish this, we have studied the dependence of the surface diffusivity to deposition conditions [cluster velocity, cluster temperature, and substrate temperature] by calculations of the spreading index $\eta(t)$ under different growth conditions (Figure 2.2). As found previously [26], $\eta(t)$ is a convenient measure of the surface diffusivity of the incident cluster and is defined as the mean-square transverse positions of the cluster atoms relative to the cluster center of mass, and can be written as

$$\eta(t) = \frac{1}{N} \sum_{i=1}^{N} \{[x_i(t) - x_{c.m.}(t)]^2 + [y_i(t) - y_{c.m.}(t)]^2\} . \qquad (2.9)$$

$x_i(t)$, $y_i(t)$, and $z_i(t)$ are the coordinates of the ith atom in the cluster at time t, whereas $x_{c.m.}(t)$, $y_{c.m.}(t)$, and $z_{c.m.}(t)$ define the dynamical position of the center of mass of the cluster. It is convenient to normalize η by the value of η for the most compact N-atom cluster of an ideal Si(111) double layer. All calculations were performed with amorphous 33-atom clusters incident on a Si(111) substrate. Biswas et al. [26] have previously estimated an optimum cluster size in the range of 30 atoms for the growth simulations. Consequently, all calculations in this work utilize amorphous 33-atom clusters.

As demonstrated by the curves 1, 2, and 3 in Figure 2.2, the initial cluster velocity is a highly sensitive parameter controlling the surface diffusivity, with the cluster spreading monotonically increasing as the cluster translational temperature (T_z) is increased from 0.35 to 2.1 eV. This temperature T_z is simply the cluster translational kinetic energy. We note from runs 1 and 2 that $\eta(t)$ does not saturate after 16×10^3 times steps (59 ps), i.e., the deposited species is still diffusing on the surface. By allowing the system to run for 32×10^3 time steps (118 ps), we find that $\eta(t)$ does reach an approximately steady-state value (Figure 2.3).

The form of $\eta(t)$ (Figure 2.2) illustrates the equilibration of the cluster atoms after deposition. During the first 5 - 6 ps, the cluster has not interacted with the substrate and hence η is constant. After 7 ps, the cluster reaches the surface and the hot cluster atoms diffuse rapidly on the surface as indicated by the sharp rise of $\eta(t)$ with time. The cooling of the cluster atoms leads to gradual slowing down of the $\eta(t)$ following by a steady-state value of $\eta(t)$ where atoms have equilibrated and are no longer diffusing. A longer equilibration time is needed for the higher velocity runs 1 and 2 (Figure 2.3). The initial slope of the $\eta(t)$ curves provides an estimate of the

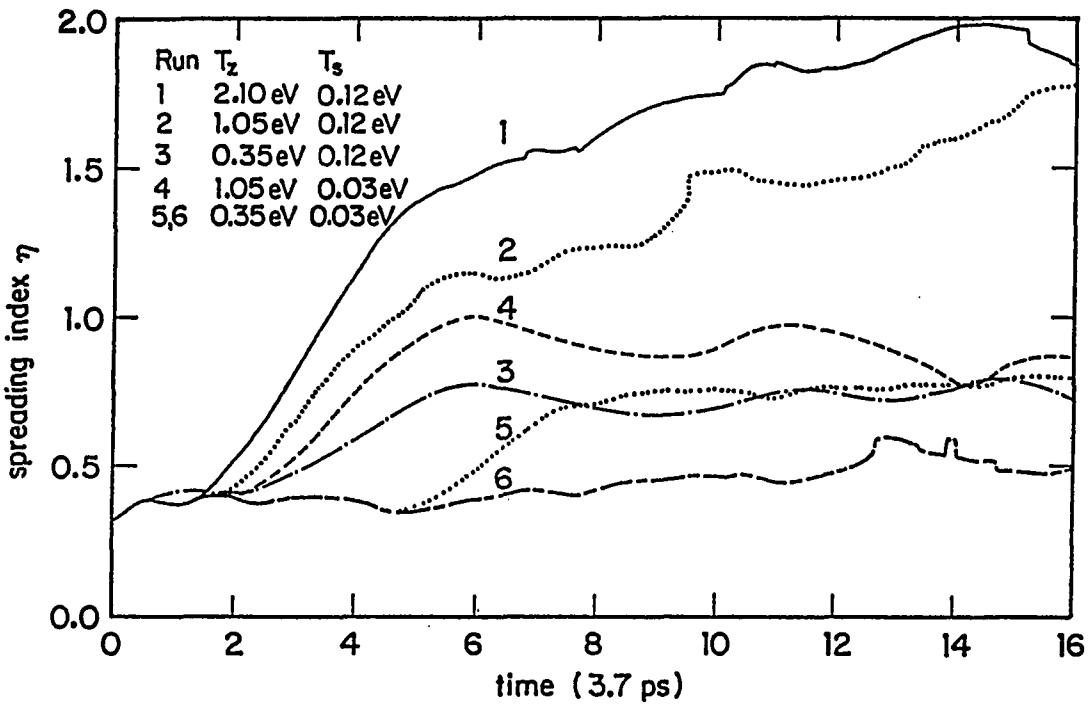

Figure 2.2: Time evolution of the normalized spreading index for 33-atom clusters. The deposition conditions, consisting of the cluster translational kinetic energy (T_z) and substrate temperature (T_s), were varied in each case

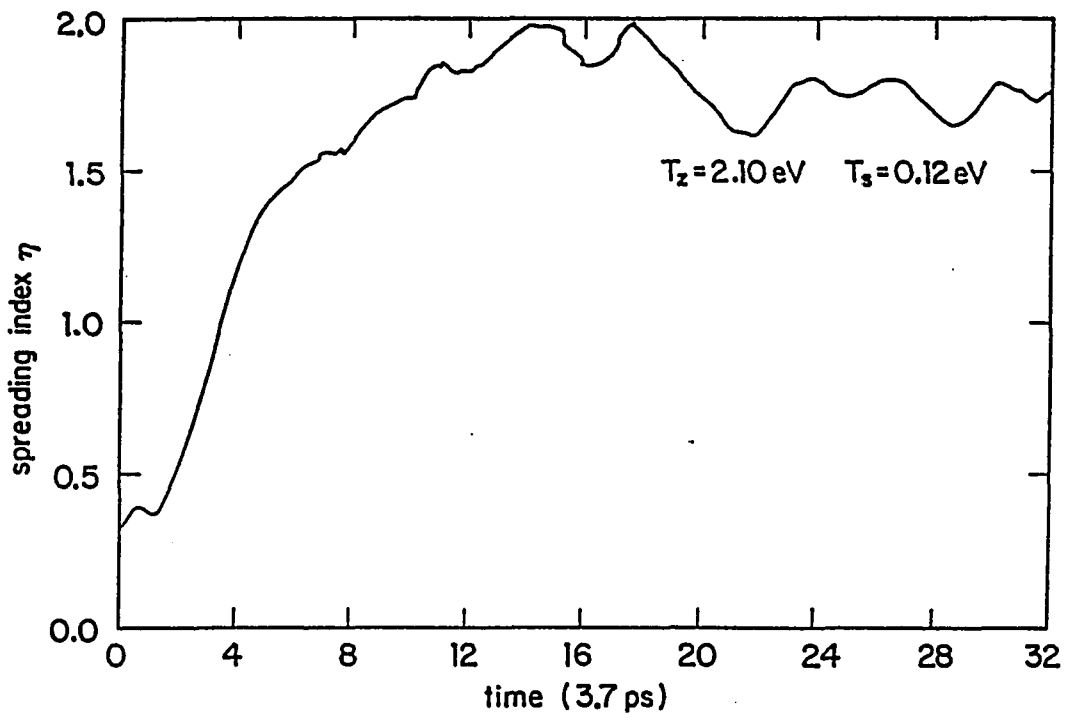

Figure 2.3: Time evolution of the normalized spreading index for 33-atom clusters with high translational temperature ($T_z = 2.1$ eV)

(initial) diffusion coefficient since the center of mass of the cluster is almost constant with time. We find (3.3, 2.1, 1.2) $\times 10^{-4}$ cm^2/s for runs 1, 4, and 3, respectively. These values compare well with both experiment and theoretical estimates and are larger than surface diffusivity values calculated for the Stillinger-Weber potential [35].

In addition, if we retain the high cluster translational temperature T_z of 1.05 eV in run 2, but reduce the substrate temperature T_s from 0.12 to 0.03 eV, the spreading of the cluster is substantially inhibited, as exhibited in run 4, Figure 2.2. This illustrates the important coupling between substrate temperatures and cluster velocities. It is, in fact, possible to achieve high surface diffusivity by lowering the substrate temperature, and increasing the incident cluster energy, a trend that is seen in experimental ICB growth studies. The low temperature growth is a real advantage of the ICB method since it allows for sharp interfaces and limits dopant diffusion.

The amorphous growth simulations in this work utilize both the low T_z (0.35 eV) and low T_s (0.03 eV) conditions for which the surface diffusivity is small as displayed in run 5 of Figure 2.2. Run 6 in Figure 2.2 shows the spreading of the cluster on an amorphous substrate with the same deposition parameters as in run 5. As anticipated, the surface diffusivity is further inhibited on an amorphous or rough substrate owing to potential wells on the surface that can trap some of the incident atoms. Run 6 is, in fact, the result for the final (14th) cluster during the growth of the a-Si film in the following section. All the other intermediate deposited clusters have diffusivities in between runs 5 and 6.

Biswas et al. [26] have previously estimated that cluster internal temperature did not have a significant effect on the surface diffusivity, and hence keep all cluster internal temperature at 0.12 eV. The cluster internal temperature is two-thirds of

the kinetic energy of the cluster in a co-moving reference frame that has the same center-of-mass velocity as the cluster. The clusters have a glassy structure. In order that the results in this work were not biased by a particular cluster structure, we used clusters that were relaxed, equilibrated fragments of bulk a-Si networks that were generated with melt-quenching molecular dynamics simulations.

Amorphous Silicon Film Growth Simulations

In this section, we utilize the deposition conditions, determined in the preceding section that lead to low surface diffusivity, to simulate the growth of an a-Si film on the Si(111) substrate. These deposition conditions correspond to a low translational energy ($T_z = 0.35$ eV) of the impinging clusters, in conjunction with a cold substrate temperature ($T_s = 0.03$ eV) which are the parameters of run 5 in Figure 2.2. Although run 3 of Figure 2.2 with a higher substrate temperature $T_s = 0.12$ eV and the same cluster velocity appeared equally suitable, the higher substrate temperature would lead to greater difficulty in keeping the deposited atoms cool, and hence the T_s of 0.03 eV was chosen. In fact, experimentally, substrate temperatures around 0.04 eV are typically used in a-Si film growth.

Following the simulations described in Figure 2.2, we chose a deposition rate of one cluster deposition every 20,000 time steps (74 ps). This time seemed adequate to allow the deposited 33-atom clusters to equilibrate with the substrate, at least for the low surface diffusivity conditions.

Two schemes were implemented in cooling the deposited atoms. In the first case, the velocities of only the 240 substrate atoms were rescaled to maintain this substrate at a constant temperature T_s of 0.03 eV. The energy transfer rate to the

substrate becomes slower as the adsorbate layer grows in thickness, resulting in the adsorbate gradually warming up during the simulation with a temperature gradient existing through the adsorbate. After deposition of 14 clusters (462 atoms), local temperature varied from $\sim$ 0.05 eV just above the substrate to $\sim$ 0.20 eV at the top surface. After deposition of the last (14th) cluster, the system was allowed to evolve for 48,000 time steps (178 ps), before rescaling the adsorbate velocities to cool the adsorbate temperature to 0.03 eV in a 120 ps run. Finally, a steepest descent relaxation led to a zero-temperature amorphous structure we label as *M1*. The total simulation time corresponded to 1.35 ns, i.e., 3.6×10^5 time steps.

In a steepest descent relaxation, each atom of any dynamical configuration is continuously displaced at a rate proportional to the force which the atom experiences until the configuration reaches to its nearby potential energy minimum. Such mapping of instantaneous system configurations to potential energy minima removes the obscuring influence of thermal vibrations away from potential energy minima and consequently produces a temperature-independent inherent structure.

In the second scheme, the adsorbate was maintained at a much cooler temperature than in the *M1* simulation, leading to substantially reduced surface diffusion. This was achieved by controlling the velocities of adsorbate atoms that were at least 3.0 Å away from the growing surface together with the velocities of the movable substrate atoms. We took care not to control the atoms at the growing surface so that the growth dynamics at the surface was not affected. As the clusters were deposited, we would periodically raise the number of control atoms. The temperature of the control atoms was maintained at the substrate temperature T_S of 0.03 eV and the control atoms were for most of the time more than 3.0 Å below the growing surface.

The result of this procedure was to have at the end of the simulation three adsorbate slabs with upper surfaces that were 11.2, 21.4, and 26.9 Å above the substrate consisting of 132, 126, and 74 atoms, respectively, that were individually maintained at 0.03 eV.

Up to deposition of the sixth cluster, the results of the previous run were used so that the amorphous layers near the substrate in this simulation were identical to *M1*. The final annealing and steepest descent relaxation were similar to the *M1* case, leading to the structure *M2*. The total simulation time was 1.08 ns, which required about 250 h of Scientific Computer Systems, Inc. SCS-40 mini-supercomputer central-processing-unit (CPU) time.

The amorphous nature of the deposited layers is displayed by the density of atoms in the perpendicular z direction (Figure 2.4). There is a remnant of crystallinity in the adsorbate immediate adjacent to the substrate ($3.0a \leq z \leq 3.30a$, $a = 4.05$ Å), but a relatively random distribution for higher z ($z \geq 4.0a$) where the structure is amorphous. This interpretation is also supported by the projected atomic positions of the first two deposited layers ($z \leq 4.30a$, or 8.1 Å above the substrate), in Figure 2.5. The first amorphous layer reveals a domain of crystalline six-membered rings. There is a void of considerable extent ($\sim$ 8 - 10 Å laterally) around which distorted five- and eight-membered ring structures exist. For the second deposited layer, crystallinity is absent and the structure is amorphous at and above this layer. The crystallinity in the interfacial deposited layer is consistent with the results of Schneider et al. [36] who also observed a similar effect in their amorphous layer generated with single-atom depositions. It is not surprising that the crystalline substrate induces an ordering directly adjacent to it.

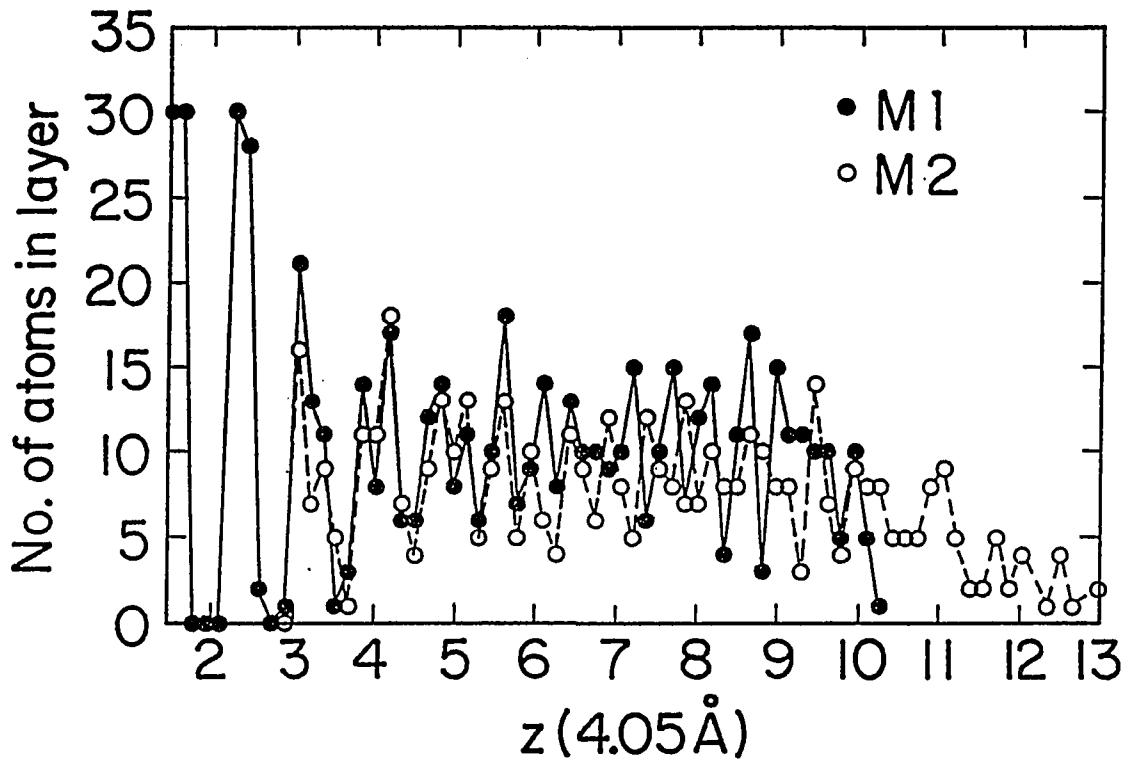

Figure 2.4: Variation of the density of deposited atoms in the z direction for two a-Si layers *M1* and *M2*. A bin size Δz of 0.65 Å has been used

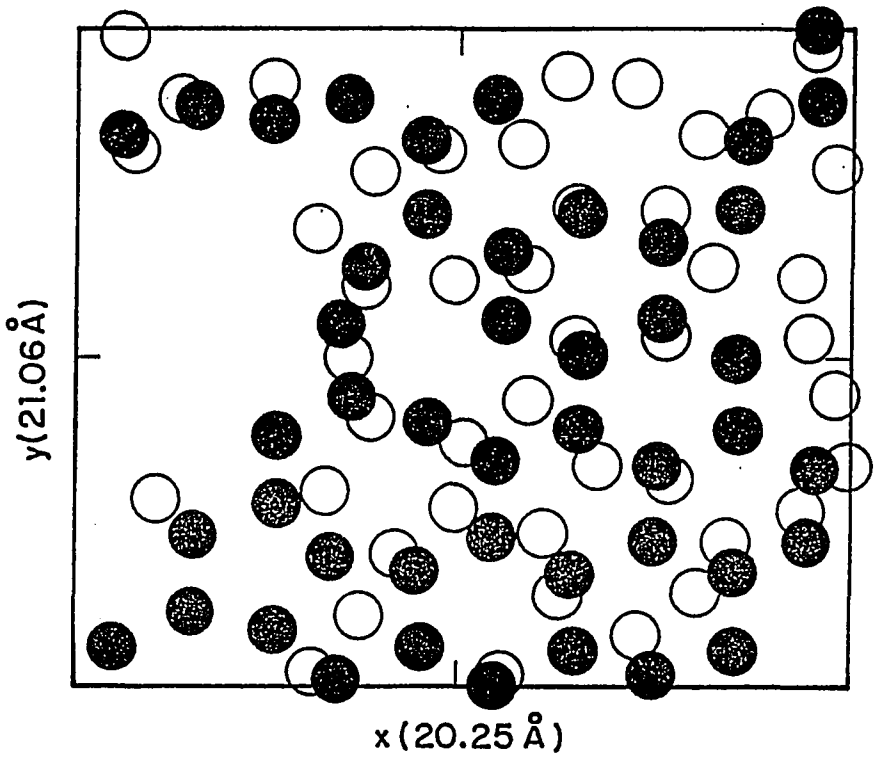

Figure 2.5: Projection of atoms of the first two layers in the x-y plane. The first layer atoms are represented by solid circles

The pair correlation function $g(r)$ of the amorphous layers (Figure 2.6) shows considerable short-range order with well-defined first and second neighbor peaks, similar to the $g(r)$ for the melt-quenched a-Si models [22] and the a-Si model generated by Wooten, Weaire, and Winer (WWW) [20] from Monte Carlo simulations (Figure 2.6). In WWW model, local atomic rearrangements are introduced into a tetrahedral structure that preserve distorted tetrahedral bonding but introduce fivefold and sevenfold rings. These local rearrangements were accepted according to a Metropolis Monte Carlo algorithm [37] with a Keating model [38] for the strain energy. A steepest-descent relaxation was needed after each Monte Carlo move. A very large number of such moves were found to effectively randomize the structure and produce pair correlation functions for the final state that compared very well with experiment for a-Si.

The pair correlation function $g(r)$ is defined such that the average number of atom centers lying between r and $r + dr$ from the center of an arbitrary origin atom is given by $4\pi r^2 g(r)dr$. Conventionally, divided by the average value of density, it is normalized to unity for very large values of r where the material becomes homogeneous. The first peak corresponds to the first shell of atoms, the second peak to the second shell, and so on. For example, the pair correlation function of crystalline Si should have the first peak at $r = 2.35$ Å, the second peak at $r = 3.84$ Å, and the third peak at $r = 4.50$ Å. In crystals, the widths of the peaks arise solely from the thermal fluctuations in the bonds. But, amorphous materials have additional brodening contributions resulting from static (topological) disorder in the bond length and in the bond angle. The Fourier transform of the structure factor gives the pair correlation function in experiments.

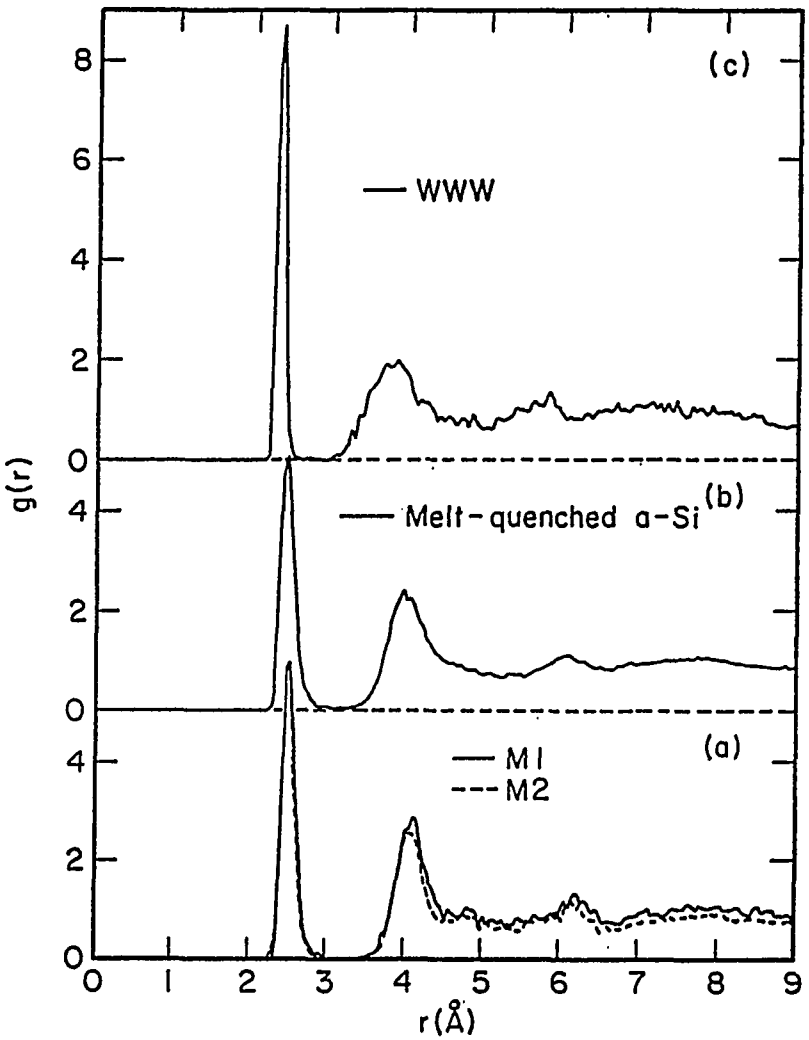

Figure 2.6: Pair correlation functions $g(r)$ for (a) amorphous states produced by cluster deposition (*M1* and *M2*), with all deposited atoms included, (b) 2000-atom amorphous system produced by melt-quenching of Si atoms [22], and (c) the continuous random-network model of Wooten, Winer, and Weaire [20], generated with Monte Carlo simulations

Contrary to a-Si models generated from the Stillinger-Weber potential [28], and in agreement with experiment, there is no shoulder in the second peak of $g(r)$, and this will be discussed later. There are fewer neighbors in between the first and second peaks of $g(r)$ in the a-Si layers than in the melt-quenched a-Si models. The first peak of $g(r)$ is somewhat sharper and stronger in the WWW model than in either of the molecular dynamics models.

The bond-angle distribution of the a-Si layers, the melt-quenched a-Si models, and the WWW model is compared in Figure 2.7. A bond cutoff of 2.94 Å, in between the first and second peaks of $g(r)$, was used to define bonds. The bond-angle distribution (Figure 2.7) reveals a narrower distribution around the tetrahedral angle for the a-Si layers than either the melt-quenched or the WWW a-Si models.

The observation of a narrower second peak of the pair correlation function $g(r)$ for the a-Si layers than for the other a-Si models (Figure 2.6) is related to the sharper bond-angle distribution for the a-Si layers. For systems in which the first-neighbor distribution is narrow, such as amorphous semiconductors including a-Si, the bond-angle distribution ($g_\theta(\theta)$) and the distribution of the second peak of $g(r)$ ($g_2(r)$) are simply related by the approximate relation

$$g_\theta(\theta) \approx g_2(r)dr_2\,, \tag{2.10}$$

because

$$r_2 \approx 2r_1 \sin(\frac{\theta}{2})\,. \tag{2.11}$$

Here, r_1 is the first nearest-neighbor bond-length, r_2 the second nearest-neighbor bond-length, and θ is the bond-angle for the first shell.

The bond-angle rms values range from 8.6° to 9.2° for the *M1* and *M2* a-Si layers (Table 2.1). These values are considerably smaller than in previous melt-quenched

bulk models where θ_{rms} ranges from 11° to 14°. A reason for this is that the voids in the a-Si layers substantially reduce the local strain. The crystalline Si(111) substrate also induces a considerable degree of ordering near the substrate (Table 2.1), which is also indicated by the six-membered rings in the interfacial a-Si layer.

A remarkable result was that there were no five-coordinated defects (floating bonds) in the amorphous silicon films. All the coordination defects instead consisted of undercoordinated atoms, primarily three-coordinated atoms (Table 2.2). This is in direct contrast to melt-quenched a-Si models generated with the same interatomic Si potential. These bulk melt-quenched models with periodic boundary conditions had 3.1 %, 10.1 %, and 3.5 % of floating bonds in the N = 216, 512, and 2000 atom a-Si models, respectively. The reason for the dramatic absence of floating bonds is closely related to the presence of voids in a-Si which will be discussed in the following section.

The distribution of dangling bonds is inhomogeneous in our a-Si layers. All the two-coordinated atoms and a larger density of dangling bonds are near the top surface, where $\sim$ 59 % of the atoms are undercoordinated. The voids in the lower amorphous layers also lead to a higher density of dangling bonds near the amorphous-crystal interface than further into the amorphous layers (Table 2.2).

Void Structures in Amorphous Silicon

A universal feature of amorphous solids is the presence of voids or macroscopic inhomogeneities in the disordered structure. For amorphous semiconductors, the characteristics of the voids are strongly dependent on the growth conditions. Structural inhomogeneities such as voids are commonly believed to result in the density

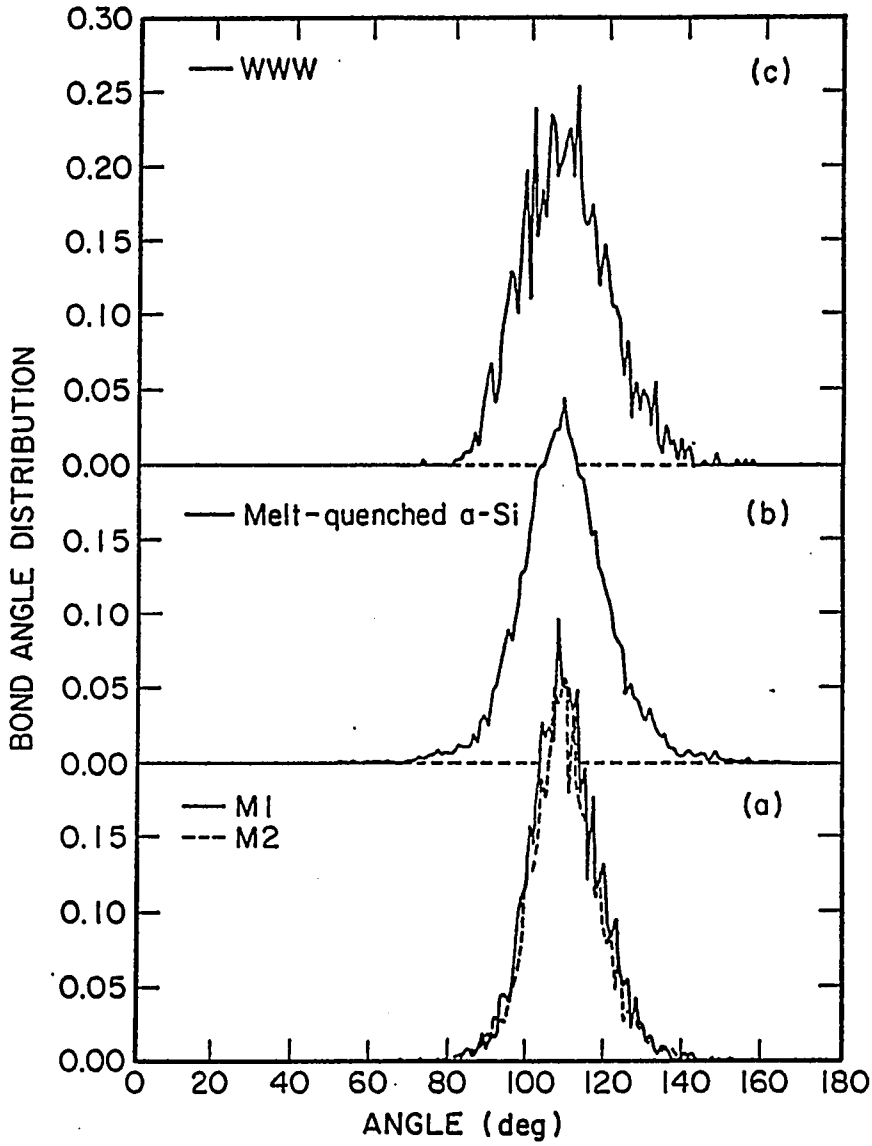

Figure 2.7: Bond-angle distributions for (a) amorphous states produced by cluster deposition (*M1* and *M2*), with all the deposited atoms included, (b) 2000-atom amorphous system produced by melt-quenching of Si atoms [22], and (c) WWW model [20]

Table 2.1: The rms values of the bond-length and bond-angle distributions with average bond-length and bond-angle values for the different a-Si layers (*M1* and *M2*). The variations with height z (Å) are also displayed

	R_{av}(Å)	R_{rms}(Å)	θ_{av}(deg)	θ_{rms}(deg)
M1 FULL	2.52	0.087	110.18	8.65
11.1< z <17.6	2.49	0.073	110.87	7.43
17.6< z <30.5	2.53	0.090	110.91	8.61
M2 FULL	2.51	0.092	110.34	9.24
11.1< z <17.6	2.49	0.073	110.61	7.86
17.6< z <30.5	2.52	0.098	110.30	9.80

Table 2.2: The number of atom N_i with coordination i in the different a-Si layers. The variations with height z (Å) are also displayed, including number of atoms N_{tot} and average coordination numbers $< N_i >$

	N_2	N_3	N_4	N_5	N_{tot}	$< N_i >$
M1 FULL	4	127	331	0	462	3.71
11.1< z <17.6	0	39	52	0	91	3.57
17.6< z <30.5	0	42	162	0	204	3.79
M2 FULL	16	181	265	0	462	3.54
11.1< z <17.6	3	35	44	0	82	3.50
17.6< z <30.5	4	56	113	0	173	3.63

of amorphous silicon or amorphous germanium being lower than their corresponding crystalline phase. The coarse microstructure and presence of voids in amorphous silicon films can be imaged with electron microscopy. The characteristics of voids in pure and hydrogenated amorphous silicon have been inferred from intense small-angle scattering of neutrons [39, 40], electrons [41], and x-rays [42, 43]. These experiments [39, 40, 41, 42, 43] measured a static structure factor $S(q)$ displaying a rapid increase for wave vector less than 1 Å^{-1}. This intense small-angle scattering was interpreted as due to a distribution of voids.

In many respects, the small-angle scattering is the only quantitative probe of the microstructure of amorphous films, and is an extremely valuable tool in identifying the changes in the film microstructure after processing steps such as annealing or light illumination. In studies of the Staebler-Wronski effect [5], for example, Chenevas-Paule et al. [40] have inferred from small-angle neutron scattering that illumination of a-Si:H with visible light leads to microstructural changes at a 100-Å scale that are reversible upon annealing.

The small-angle scattering is a measure of the long-wavelength density fluctuations in the amorphous material. If this scattering is assumed to be due to voids that can be represented by an average radius of gyration R_G, the $q \rightarrow 0$ scattering intensity is given by the Guinier relation [44],

$$S(q) = S_0 \exp(-\frac{q^2 R_G^2}{3}). \tag{2.12}$$

For small-angle-scattering data, Guinier plots of $\ln[S(q)]$ versus q^2 reveal approximate linear relationships over ranges of q, from which radii of gyration ranging from 270 to 5 Å have been estimated [39, 40, 41, 42, 43]. Although this intense small-angle scattering has been seen with a number of different probes, there has been little the-

oretical modeling of this scattering. In fact, it is not known if theoretical structural models can support the presence of voids and can account for this small-angle scattering in a-Si. In this section, we investigate whether theoretical a-Si models can describe the intense small-angle scattering found experimentally.

Voids in Bulk Melt-Quenched Amorphous Silicon Networks

We start with a-Si models generated by Biswas, Grest, and Soukoulis (BGS) [22] from molecular dynamics simulations, resulting in N-atom models (N = 512 and 2000) with periodic boundary conditions. The molecular dynamics simulations were performed with the Biswas-Hamann interatomic Si potential [30]. This potential is more complicated than is necessary for calculating vibrational properties, and its parameters were not optimized to fit vibrational data. For determining phonon densities of states, we adopted the Keating model [38] with bond-stretching and bond-bending force constants (α and β). The Keating potential energy is given by

$$V = \frac{3\alpha}{16d^2}\sum_{i,l}(\vec{r}_{il}\cdot\vec{r}_{il} - d^2)^2 + \frac{3\beta}{8d^2}\sum_{i,j,l}(\vec{r}_{il}\cdot\vec{r}_{jl} + \frac{1}{3}d^2)^2, \qquad (2.13)$$

where d = 2.35 Å is the equilibrium bond-length of Si in the diamond structure. The first sum in the expression is on all atoms i and their nearest neighbors specified by l; the second sum is on all atoms and pairs of distinct neighbors. Monte Carlo calculations at zero temperature were used to relax the BGS networks with the Keating potential using the parameters of α = 42.1 N/m and β/α= 0.16. The change in the atomic positions was minimal as a result of this additional relaxation step, which led to a local minimum with the Keating potential energy.

The Keating-model calculations of the vibrational densities of states of the a-Si

models [45, 46] compares well with experiment [47] (Figure 2.8), describing the TA and TO peaks well. The coordination defects in these models have led to predictions [45] for localized vibrational models at both high and low frequencies. The calculated structure factor $S(q)$ (Figure 2.9) smoothly approaches zero as $q \rightarrow 0$, illustrating the homogeneity of the amorphous network. The structure factor $S(q)$ is defined by

$$S(q) = \frac{1}{N} \mid \sum_{i=1}^{N} e^{i\vec{q}\cdot\vec{R}_i} \mid^2, \tag{2.14}$$

where $\vec{R}_i$ is a atomic position vector and N is the number of atoms in the system.

The columnar growth of a-Si films [48, 49, 50, 51, 52] often leads to void structures that are somewhat ellipsoidal in nature. Due to the finite size of our models, columnar voids are difficult to model. As a first step toward understanding the properties of voids in a-Si, we have chosen to study the properties of simple spherical void structures, which can be easily generated. As the results of this work indicate, many experimental features of the scattering can be understood from the simple spherical multivoid structures.

We found that a simple way to generate approximately symmetrical voids in the amorphous network was to remove a cluster starting with an atom selected at random and its shell of the first neighbors. The neighbors of this first shell were removed and the process extended up to m shells around the central site. With this simple procedure, much fewer bonds are broken than by removing atoms within some prescribed volume. By choosing the centers of the voids to be sufficiently far apart, a number of nonoverlapping voids were then constructed.

The void structures were relaxed by a steepest descent relaxation with the Si interatomic potential [30], which led to a rebonding of atoms at the void surfaces. The

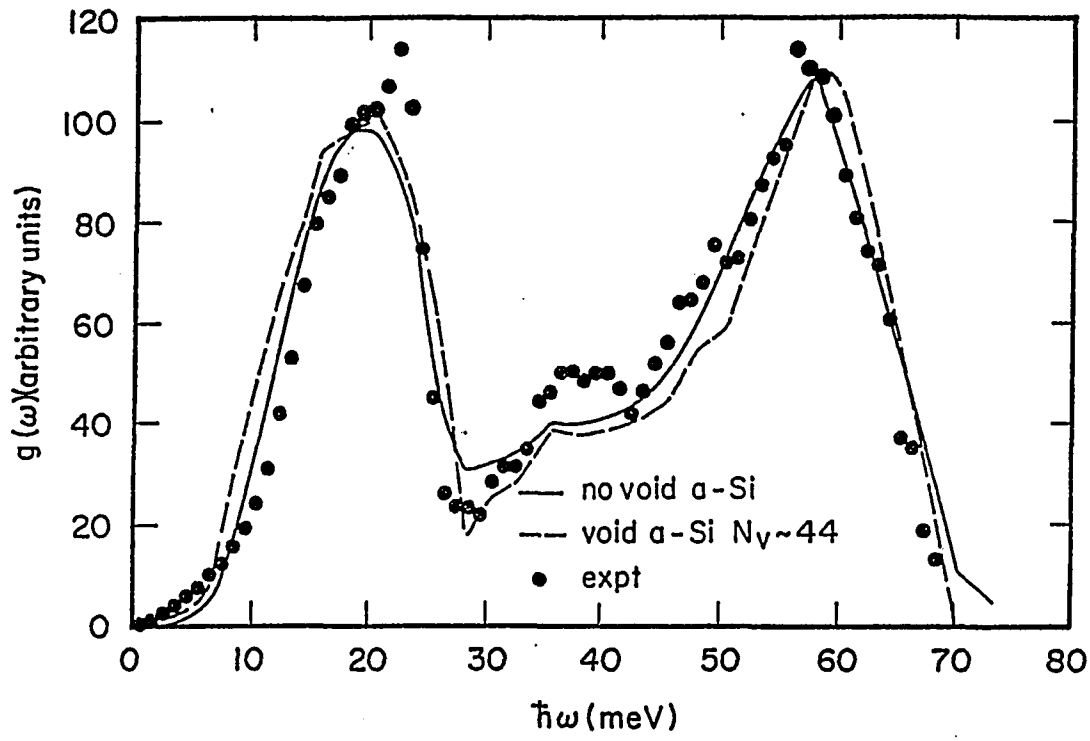

Figure 2.8: Vibrational densities of states for a-Si models - without voids ($N = 512$ atoms, solid line), with voids of average size 44 atoms and with $N = 380$ atoms. Experimental points are from Kamitakahara et al. [47]

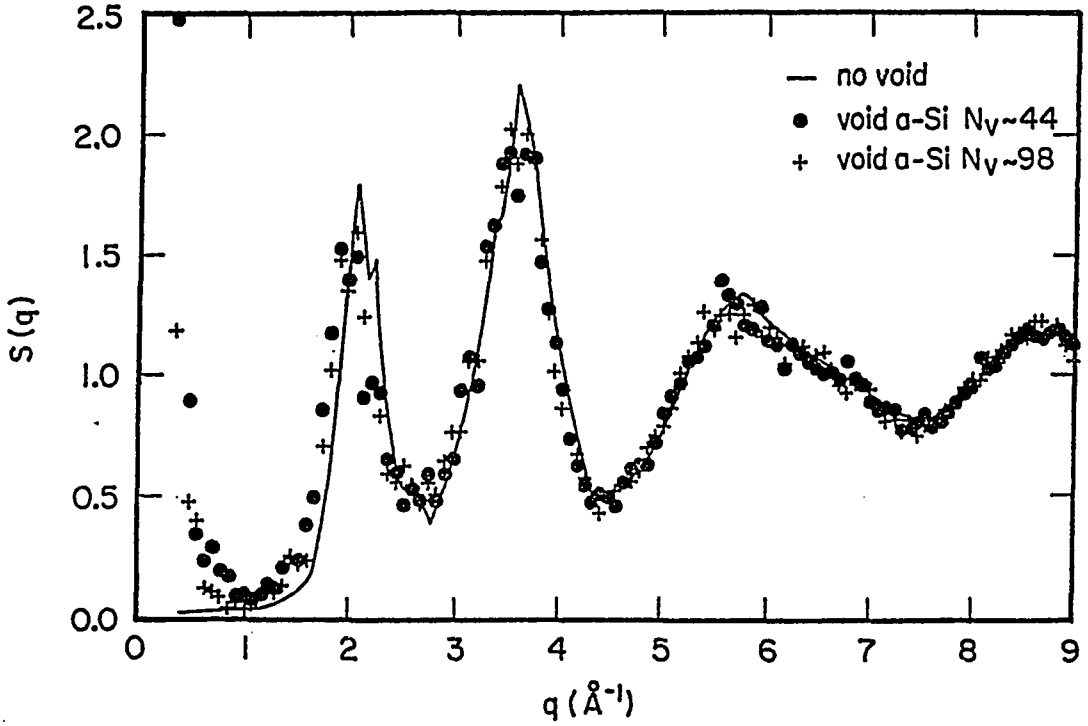

Figure 2.9: Static Structure factor $S(q)$ for a-Si models without voids (solid line) compared with a-Si models with void sizes of N_v atoms (points)

Keating potential was not used in this step since it preserves the local coordination of the atoms. Relaxation of the a-Si networks with the Si interatomic potential was a much more efficient way to achieve rebonding at the void surfaces. After the steepest descent relaxation, we equilibrated the a-Si models with the Keating potential with Monte Carlo calculations at zero temperature, which resulted in a minimal change in atomic positions. The Keating equilibration calculation was performed at different densities, and we found that somewhat lower atomic volumes were energetically favored for the networks with voids. The equilibration with the Keating model was necessary to consistently compare vibrational densities of states calculations with the previous results for a-Si models without voids. We stress that the models with voids are not hypothetical high-energy configurations, but are energetically competitive with the starting amorphous network. The a-Si model without voids (model 6 in Table 2.3) had an energy of -3.377 eV/atom compared to -3.398 and -3.388 eV/atom for models 7 and 8, which had voids. These energies were computed after the steepest descent relaxation step with the Si interatomic potential.

Average void sizes (N_v) of 17, 44, and 98 atoms were constructed with values of m of 2, 3, and 5, respectively (Table 2.3). The vibrational densities of states (Figure 2.8) displayed only small changes with the introduction of the voids. A noticeable feature is the loss of modes between 28 and 32 meV for the networks with voids, so that the density of states (DOS) has a much deeper minimum after the TA peak (Figure 2.8). Consequently, a more well-defined peak at 35 meV appears, which is the analog of the crystalline LA peak. We interpret the excitations between 28 and 32 meV to be analogous to the longitudinal-acoustic phonons of the crystal with wavelengths in the range (2 - 4)a, where a is the crystalline lattice constant (5.431 Å). These modes are

unable to propagate through the network when the spacing between the voids is of the order of the wavelength of these modes, leading to decrease of such modes for the networks with voids. In fact, the introduction of voids lead to calculated DOS's that are in qualitatively better agreement with the experimental data [47] than that of the original network [45, 46]. The density of the a-Si network with the voids is somewhat less than that of crystalline Si (c-Si), in agreement with experimental measurements of the density of a-Si. In contrast, the original a-Si model had a higher density than c-Si.

The strain in the amorphous network is somewhat relieved by the presence of voids, as illustrated by the somewhat lower bond-angle deviations for the networks with voids (Table 2.3). The relief of the local strain by the voids is also illustrated by the substantial decrease in the number of five-coordinated atoms for the networks with voids (Table 2.4). The decrease in five-coordinated sites to a density below 1 % from an initial density of 10 % is the most evident in models with large numbers of voids (models 2 and 3, Table 2.4). In the studies with the Stillinger-Weber potential, Luedtke and Landman [23] inferred that floating-bond sites lead to large bond-angle strains including small bond-angles near 60° and 80°. These bond-angles near 80° also led to a shoulder in the second peak of $g(r)$ in a-Si models generated with the Stillinger-Weber potential.

The reason for the decrease in the density of floating bonds by almost an order of magnitude is closely related to the dramatic absence of floating bonds in a-Si films described in the previous section. Our interpretation is that the floating bonds can easily migrate from site to site by a bond-switching mechanism proposed by Pantelides [4]. In the presence of either the internal surfaces of voids or the external

Table 2.3: The structural characteristics and local disorder of a-Si models with voids

a-Si model	No. of atoms, N	Average void size $< N_v >$	No. of voids	No. of shells, m	θ_{rms} (deg)	r_{rms} (Å)
1	512	0	0		11.60	0.044
2	414	98	1	4	10.96	0.043
3	380	44	3	3	10.53	0.040
4	429	17	5	2	10.94	0.044
5	463	5	10	1	11.19	0.046
6	2000	0	0		10.92	0.054
7	1696	43	7	3	10.56	0.052
8	1565	87	5	4	10.83	0.059

Table 2.4: The number of atoms N_i with coordination i in a-Si models with voids, compared with the a-Si models without voids

a-Si model	No. of atoms, N	Average void size $< N_v >$	No. of voids	N_2	N_3	N_4	N_5
1	512	0	0	1	34	425	52
2	414	98	1	2	69	338	5
3	380	44	3	2	101	276	1
4	429	17	5	1	77	348	3
5	463	5	10	1	50	386	26

growing top surface of the amorphous layer, the floating bonds can easily migrate to these surfaces and then recombine with the large number of dangling bonds at these surfaces. This is consistent with the arguments of Phillips [31] that the kinetics of film growth from a vapor phase, and the presence of internal surfaces, should favor undercoordinated defects rather than overcoordinated defects.

The most significant effect of the voids is to cause a rapid increase in the static structure factor $S(q)$, for wave vectors less than 1 Å^{-1} (Figure 2.9), with negligible changes for larger q. The rapidly increasing structure factor below 1 Å^{-1} is seen for average void sizes of 98 and 44 atoms (Figure 2.10). The increase in $S(q)$ is barely perceptible for the 17-atom voids and not shown separately in Figure 2.10. The finite size of the periodic unit cell leads to a cutoff for the smallest wave vector in the calculation, which is 0.28 - 0.30 Å^{-1}, for the networks in Figure 2.10.

In Figure 2.11, we plot our results for $S(q)$ with an average void size N_v of 44 atoms, together with the experimental results of Postol et al. [39]. The agreement is impressive in the entire q region. For very low q, our calculated $S(q)$ is larger than experiment. It is worth noting that the second peak of $S(q)$ is higher than the first peak, similar to experiment. Amorphous silicon models from Monte Carlo simulations [20] had the first peak of $S(q)$ much higher than the second peak [22], indicating excessive long-range order in the Monte Carlo models. Calculated $S(q)$ for a-Si models compare well with experiment in the large-q region ($q \geq 1.5$ Å^{-1}), as discussed by other authors [21, 53].

A Guinier plot of $\ln[S(q)]$ as a function of q^2 (Figure 2.12) for the void structures constructed from the $N = 512$ model reveals approximate linear relationships for $q \leq 0.8$ Å^{-1}, although there is a considerable scatter. The scatter in Figure 2.12

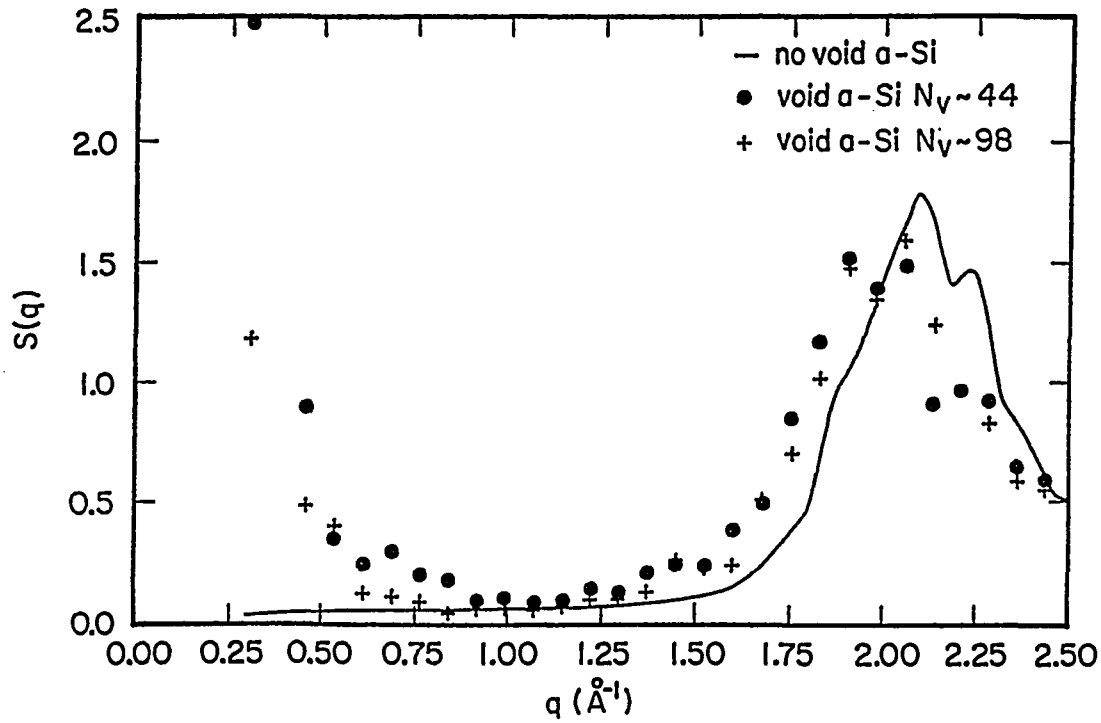

Figure 2.10: Small wave-vector region showing the rapidly increasing structure factor for a-Si models with average void sizes of N_v atoms (points), compared to a-Si model without voids

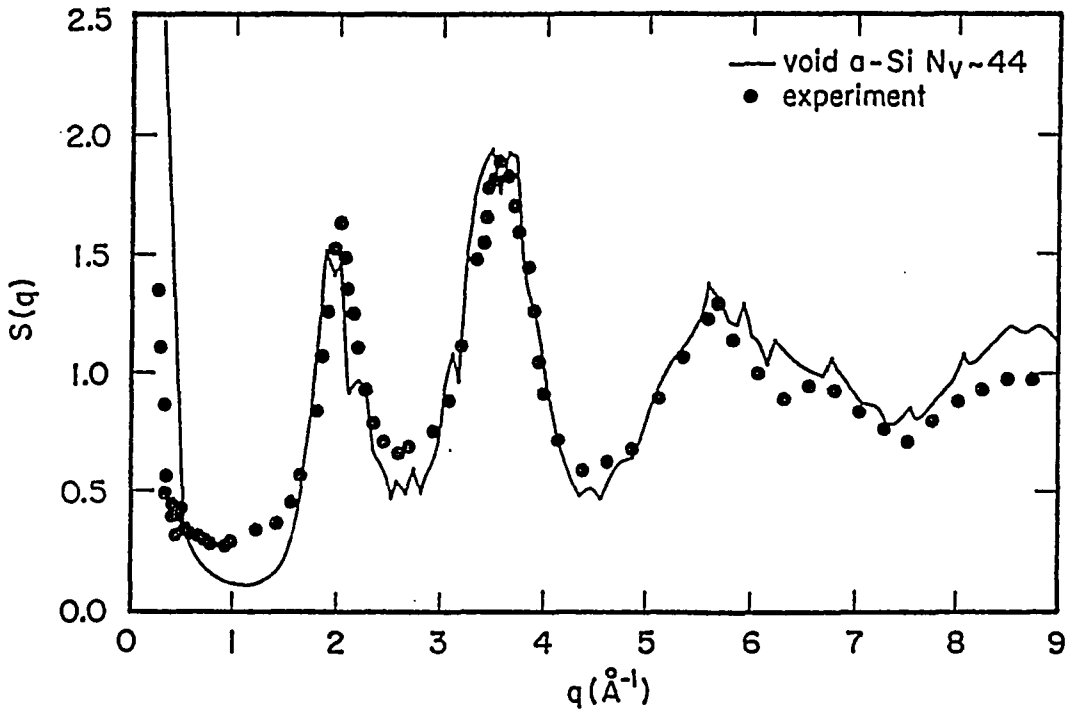

Figure 2.11: Structure factor $S(q)$ for a-Si models with voids compared to experimental data from Postol et al. [39]. The results for $S(q)$ for $N_v = 98$ were very similar and not shown separately

may be a result of the nonspherical nature of the voids since the removed atoms are not distributed symmetrically around the central site. We expect that the scatter would be less significant for larger void sizes where the variations at the boundary have less effect on the void size. From the slopes in Figure 2.12, and assuming Eq. (2.12) holds, we extract void radii (R_G) of 4.53 Å ($N_v = 98$) and 3.94 Å ($N_v = 44$), which are somewhat smaller than the void radii of 5.26 and 4.16 Å expected for crystalline Si (i.e., the fourth- and third-neighbor distances) at the same density as our a-Si model. The relaxation of the structure may be lead to a compression in the volume of the individual voids.

We confirmed that the large scattering was independent of the amorphous network used by calculations for the larger 2000-atom network, where a larger number of voids (of 43- and 87-atom size) was possible (Table 2.3). Owing to the large size of the dynamical matrix, the vibrational DOS could not be explicitly calculated for this network. The calculated $S(q)$ (Figure 2.13) shows very similar trends as the smaller networks, including an abrupt increase for $q \leq 0.75$ Å^{-1}. The larger scatter of the $S(q)$ in the small-q region may be a result of substantial variations in the void size.

Voids in Amorphous Silicon Film Networks

We have quantitatively characterized the properties of the voids in a-Si layers grown by depositions of Si clusters on Si(111) substrate by calculating the structure factor $S(q)$ for wave vectors q parallel to the surface (Figure 2.14). Both the first 13 Å of the *M1* and *M2* structures display a rise in $S(q)$ below 1.0 Å^{-1} [Figure 2.14(a)], whereas for the next 13 Å a rise in $S(q)$ is only displayed by *M2*, but not *M1* [Figure 2.14(b)]. The larger $S(q)$ at small q for *M2* suggests that there are larger

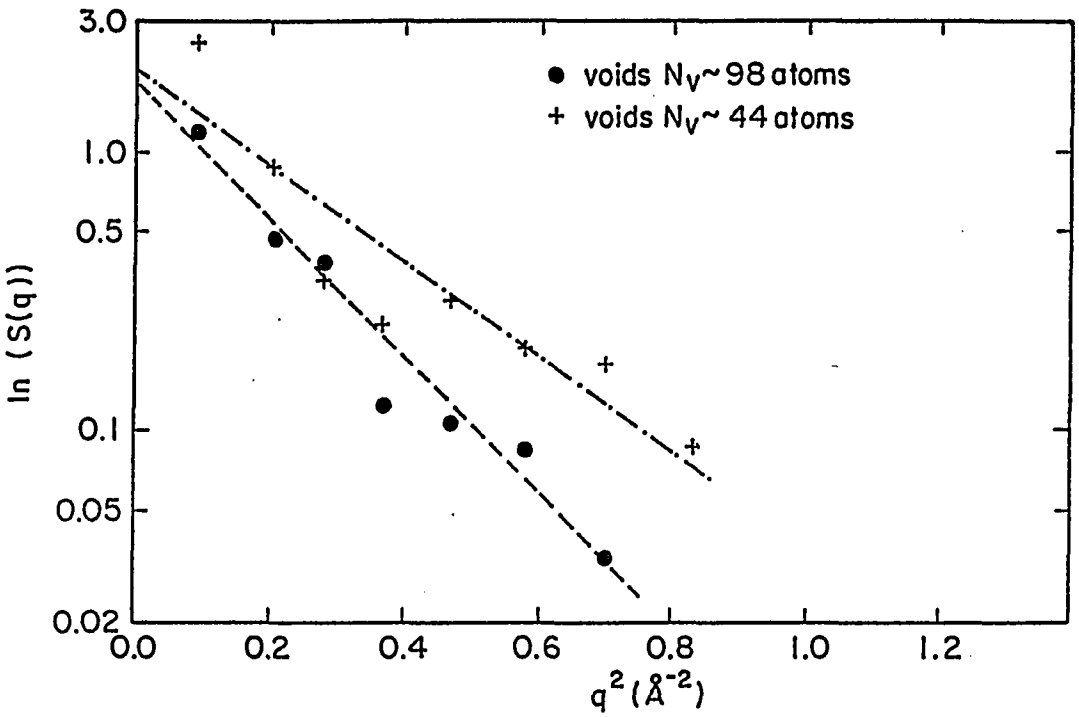

Figure 2.12: Guinier plot of the logarithm of the structure factor as a function of q^2. Only the rapidly increasing $S(q)$ due to scattering from voids for $q < 0.9$ Å^{-1} is shown. Approximate straight line fits to the calculations are shown

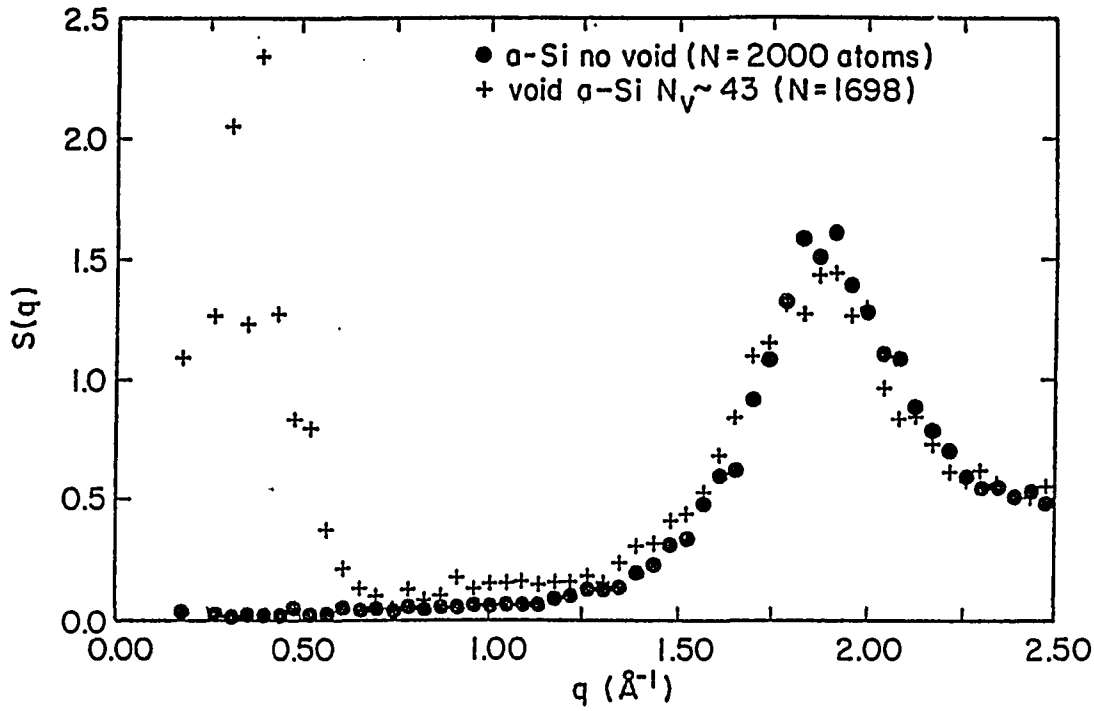

Figure 2.13: Small wave-vector region showing the rapidly increasing structure factor for a-Si model with average void size N_v, compared to the a-Si model without voids (with $N = 2000$ atoms). The void structure were derived from the $N = 2000$ atom a-Si model

voids in *M2* than in *M1*. Further, the next 13 Å of *M2* reveals voids, whereas no voids are evident in the corresponding part of *M1*. This was because the adsorbate temperature in the *M1* simulation was high enough in the later part of the growth to allow for appreciable surface diffusion that prevented voids from forming in the later stages of growth away from the substrate. *M2* has a potential energy of ~ 0.9 eV/atom higher than the *M1* structure because of the higher density of voids and consequently dangling bonds in *M2*. This is also consistent with *M2* having a lower density ($\rho = 0.72$) than *M1* ($\rho = 0.85$), in units where the crystal has a density of 1.

The voids in the *M2* structure have a qualitatively similar structure factor $S(q)$ as those of the bulk a-Si models with voids [Figure 2.14(c)], particularly for the small wave-vector scattering. The shift in the peak positions in Figure 2.14(c) is due to the lower density of the *M2* film structure than of the bulk model. A radius of gyration, R_G, of 3.6 Å, was extracted from the Guinier plot (Figure 2.15) for *M2*. This void radius of gyration is consistent with an analysis of the average positions of the atoms. From real-space plots of the projected atom positions as a function of height z, we inferred ellipsoidal void shapes, and estimated void radii of 4.0 Å in the x,y plane and 3.2 Å in the z directions, leading to a similar R_G of 3.7 Å.

These results for the void properties are inferred from two separate simulation runs. In another simulation where five clusters were deposited under similar growth conditions, we also observed a void with a spatial extent similar to the *M2* run. The large amount of CPU time required [$\sim$ 250 h SCS 40 CPU time] made further full simulations of a-Si film growth unfeasible. Biswas et al. [26] have previously reported the initial stages of cluster-induced growth under a number of initial conditions. We expect that a set of initial conditions different from the *M2* run would also produce

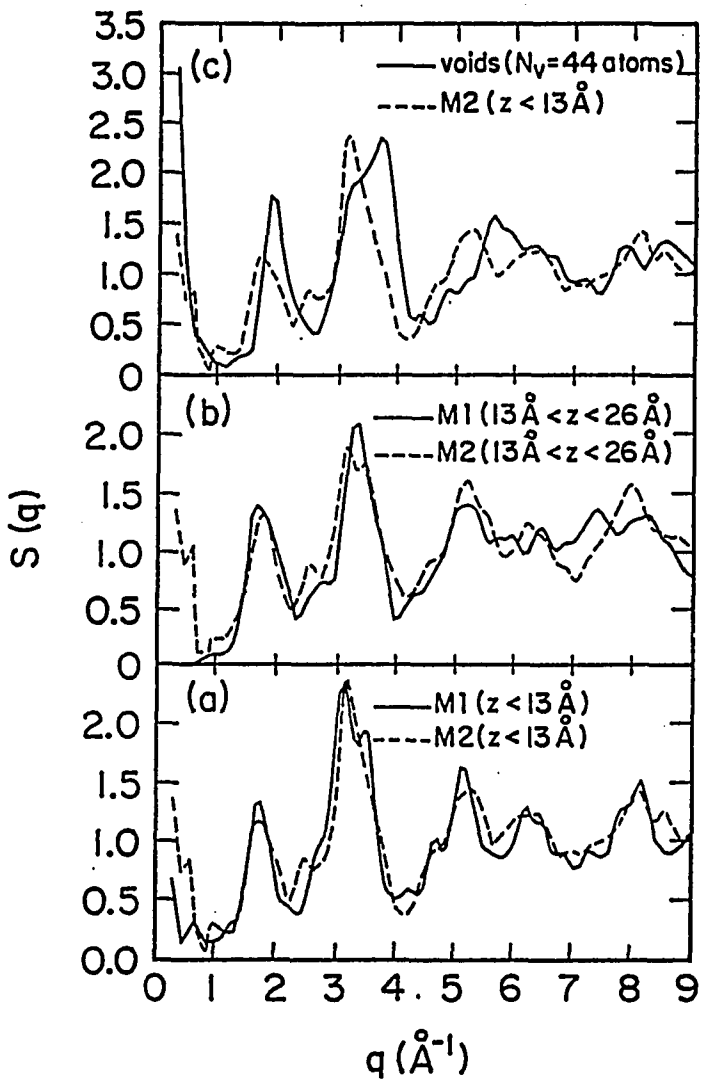

Figure 2.14: Static structure factor $S(q)$ for wave vectors q parallel to surface for the lower and upper layers of the amorphous states produced by cluster deposition [(a) and (b)], compared to the bulk a-Si model with voids [(c)]

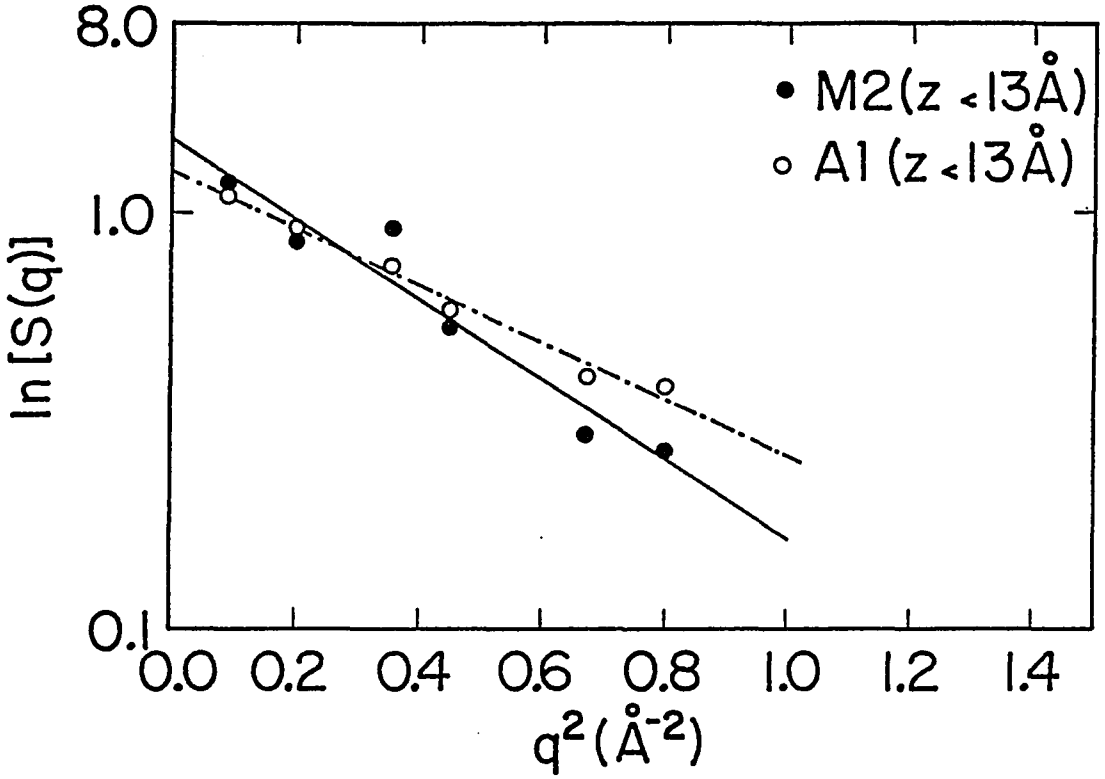

Figure 2.15: Guinier plot of the logarithm of the structure factor as a function of q^2. Only the rapidly increasing $S(q)$ due to scattering from voids for $q < 0.9$ Å^{-1} is shown. The straight lines are drawn by least-squares fitting of the data

voids with a different location that have a qualitatively similar spatial extent. We do expect the size of the voids to decrease if small clusters are used for the deposition. In fact, Luedtke and Landman [54] have report the growth of a-Si layers by deposition of single atoms using the Stillinger-Weber potential. In their simulations, microvoids in the a-Si layers were obtained when the impinging atoms were incident at random directions to the substrate, whereas a columnar microstructure of the film was found for a beam directed at 60^{o} from the normal to the substrate. However, for deposition of single atoms directed normal to the substrate, a uniform a-Si film without microvoids was generated.

With a view toward improving the structural quality of the a-Si films, we annealed the *M2* film and studied structural changes. The annealing comprised of equilibrating the *M2* model at an elevated temperature T_a for 20,000 time steps and then cooling the model at the rate of 0.01 eV per 530 time steps to a cold temperature of 0.03 eV, and a steepest descent relaxation. Two annealing temperatures T_a of 0.12 and 0.20 eV were investigated and resulted in annealed models *A1* and *A2*, respectively (Table 2.5). Both anneals led to a densification of the structure with densities (ρ) of 0.725 for *A1* and 0.756 for *A2*, compared with 0.72 for the initial *M2* structure. The densification was due to the reduction in the number and size of the voids. This interpretation is supported by the Guinier plot (Figure 2.15) for the first 13 Å of the layers, which displays a reduction in the lateral void size from $\sim$ 3.6 to $\sim$ 3.1 Å. On the other hand, the interfacial voids in both *A2* and *M2* appeared very similar. Analysis of the second 13 Å of the deposited layers of *A2* revealed that the voids in the upper layer of *M2* had been annealed away as evidenced by the lack of small wave-vector increase in $S(q)$ (Figure 2.16).

Table 2.5: The rms values of the bond-length and bond-angle distributions with average bond-length and bond-angle values for the annealed a-Si layers (*A1* and *A2*). The variations with height z (Å) are also displayed

	R_{av}(Å)	R_{rms}(Å)	θ_{av}(deg)	θ_{rms}(deg)
A1 FULL	2.50	0.087	110.52	8.99
11.1< z <17.6	2.49	0.078	110.83	8.41
17.6< z <30.5	2.51	0.089	110.43	9.26
A2 FULL	2.51	0.093	110.72	9.37
11.1< z <17.6	2.51	0.085	110.62	8.27
17.6< z <30.5	2.52	0.092	110.75	9.75

Table 2.6: The number of atom N_i with coordination i in the annealed a-Si layers. The variations with height z (Å) are also displayed, including number of atoms N_{tot} and average coordination numbers $< N_i >$

	N_2	N_3	N_4	N_5	N_{tot}	$< N_i >$
A1 FULL	16	180	266	0	462	3.54
11.1< z <17.6	1	37	48	0	86	3.55
17.6< z <30.5	3	60	107	0	170	3.61
A2 FULL	15	195	252	0	462	3.51
11.1< z <17.6	1	35	50	0	86	3.57
17.6< z <30.5	1	74	109	0	184	3.59

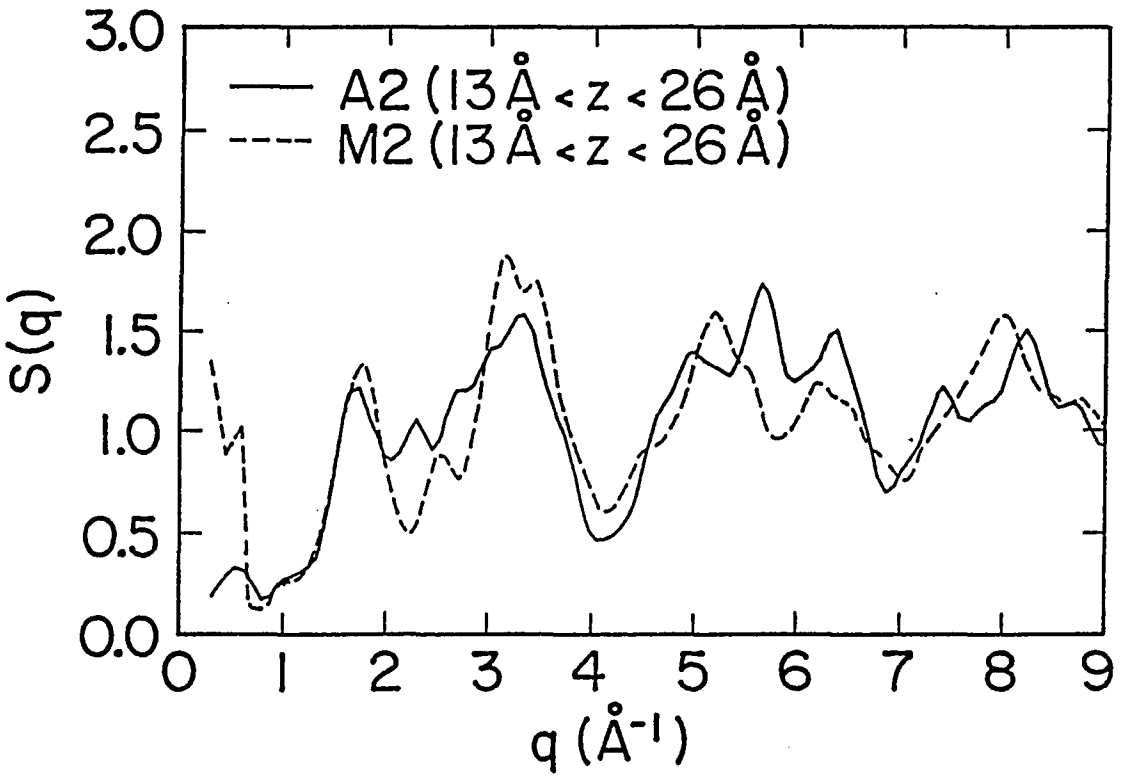

Figure 2.16: Static structure factor $S(q)$ for wave vectors q parallel to surface for the annealed a-Si state ($A1$), compared to the original a-Si state ($M2$)

CHAPTER 3. STRUCTURAL MODELING OF HYDROGENATED AMORPHOUS SILICON

Pure amorphous silicon thin films generated by sputtering or glow-discharge methods exhibit a large ESR signal ($\sim 10^{19}$ - 10^{20} spins cm^{-3}). While the origin and properties of the paramagnetic defect spins, commonly believed as dangling bonds, are interesting in themselves, they generally obscure many phenomena of interest in semiconductor physics. For example, the electron energy levels of the defect spin lie in between the valence (bonding) states and conduction (antibonding) states of the fully paired, bonded electrons. These states in the gap contribute to optical absorption and electrical conduction processes, masking the measurement of an energy gap by either process. Further, there is a large density of gap states which act as efficient non-radiative recombination centers, with the result that photoconductivity or photoluminescence is uninterestingly small in pure amorphous silicon. Finally, the Fermi level, which is essentially pinned by the gap states, does not move significantly when trace impurities of conventional shallow donor or acceptor type (e.g., phosphorus (P) or boron (B), respectively) are incorporated. Impurities will donate or accept an electron to or from the defect gap states, but the density of states is so high and the number of impurity atoms so relatively small, that the Fermi level is not shifted significantly and the material is not doped.

Normally, annealing procedures reduce the ESR signal and the tailing of the optical absorption edge. However, amorphous silicon will crystallize before all the defects are removed either by annealing or by slowly depositing onto substrates at elevated temperatures.

This is not the case for hydrogenated amorphous silicon, prepared for example by the glow-discharge decomposition of silane, which have such a low residual density of gap states (as low as $\sim 10^{15}$ cm^{-3}) that the substitutional introduction of P, As, or B can easily dope the materials n- or p-type, changing the electrical conductivity by many orders of magnitude [55]. Presumably, the presence of the hydrogen acts in the main part to satisfy any dangling bonds, thereby removing the defect states in the gap, replacing them with Si-H bonding states deep in the valence band, and rendering the material dopable.

Many intrinsic properties of hydrogenated amorphous silicon have been studied to date, including the thermally activated conductivity, the optical absorption edge, photoluminescence, electroluminescence, and photoconductivity, in addition to doping of the materials. The phenomena and configurations of interest and import to single crystal silicon, now become amendable to study with amorphous silicon. Extrinsic conductivity, thermopower, Hall effect, and photoconductivity, amongst others, are all dopant-dependent phenomena with crystalline analogs that have been measured for amorphous silicon. Often the results are interpretable in terms of processes previously described for crystals. Sometimes - the sign of the Hall effect has been the most notable example - the crystalline analogy does not work. Schottky barrier and the *pn* junction are two device-like configurations that have been constructed with amorphous silicon. When operated as solar-cells, these diodes behave

to some extent like the corresponding crystal devices.

Besides passivating gap states, hydrogen might play an active role by enlarging the band gap (alloying with Si), sensitizing photoexcited processes, changing the lattice-electron coupling, etc. The introduction of H progressively erodes the top of the valence band as well as removing states from the gap, as shown by photoemission studies and the finding that the optical gap increases on hydrogenation by $\simeq$ 0.4 eV for $\simeq$ 15 at.% H [56]. How much hydrogenation is needed to reveal the most interesting phenomena is still an open question. It is found that some 10 times more H ($\simeq$ 1 - 10 at.%) is introduced by the glow-discharge process into a-Si:H than is needed to satisfy all the dangling bonds evidenced by ESR in evaporated a-Si; indeed, NMR experiments [57] and calorimetric experiments [58, 59] have demonstrated that about 5 % of the hydrogen in a-Si:H occurs in the form of molecular H_2 trapped in microvoids in the matrix of amorphous silicon. The role of hydrogen in the deposition process and the subsequent electrical activity of this potentially useful electronic material is still a subject of some considerable controversy and active study.

Although the importance of a-Si:H to photo-voltaics and other applications is well recognized through extensive experimental studies, theoretical models of a-Si:H are a few in contrast to pure a-Si models [20, 21, 22, 23, 27, 54, 60]. One reason is the difficulty in modeling the interatomic Si-H interactions. There is a class of a-Si:H structures generated by the saturation of dangling bonds in pure a-Si [61] or built by hand [62] and then relaxed by Keating-type potentials for both H atoms and Si atoms. A drawback of these models is that structural and vibrational properties of the a-Si:H networks can be studied only by static calculations. Recently however, Chiarotti et al. [63] have performed ab-initio molecular dynamics simulations to investigate static

and dynamic properties of H in crystalline Si and a-Si based on the Car-Parrinello approach. Such ab-initio molecular dynamics calculations are more accurate but far less efficient for simulations for either long times or large systems than classical molecular dynamics. Mousseau and Lewis [64] have developed a-Si:H networks using a Stillinger-Weber type interatomic potential for bonded H but a different form of potential for non-bonded H.

In this chapter, we have studied structural modeling of a-Si:H with molecular dynamics simulations. A new classical interatomic potential for Si-H interactions has been developed and used in conjunction with the previous interatomic potential model for Si-Si interactions.

Interatomic Potentials

Although there have been extensive developments of classical interatomic potential models for Si-Si interactions [28, 29, 30], the modeling of interatomic potentials for Si-H interactions is in an early stage of development. A difficult problem in Si-H potential models is to ensure the monovalency of H. Recently, Mousseau and Lewis [64] have developed a Stillinger-Weber type interatomic potential for Si-H interactions to construct a computer-generated a-Si:H model. Although some structural and dynamical properties of a-Si:H networks developed with this potential agree well with experimental measurements, they used different potentials for bonded H-Si pairs and non-bonded H-Si pairs, which generally makes molecular dynamics simulations difficult, particularly at finite temperature, where atomic environments can change. We have instead developed a set of two- and three-body interatomic potential that can describe the energy of any arbitrary configuration of Si and H atoms without

the need to classify bonded and non-bonded H-Si pairs. Although we study a-Si:H in this work, we believe that the interatomic potential developed here could be useful for other Si-H systems as well.

Following previous classical models of Si-Si interactions [30], we partition the Si-H interaction into a sum of two- and three-body interactions. The two-body potential for Si-H interaction is

$$V_2^{Si-H}(r) = [C_1 \exp(-\kappa_1 r) + C_2 \exp(-\kappa_2 r)] g_c(r)\,, \tag{3.1}$$

where $g_c(r)$ is the cut-off function,

$$g_c(r) = \begin{cases} 1 & \text{for } r \leq 1.70\mathring{A} \\ 0.5 + 0.5\cos[\frac{\pi}{0.2}(r - 1.7)] & \text{for } 1.70\mathring{A} \leq r \leq 1.90\mathring{A} \\ 0 & \text{for } r \geq 1.90\mathring{A} \end{cases} \tag{3.2}$$

The parameters [65] were obtained by fitting to ab-initio calculation of the energy of H on a Si cluster [66]. This two-body potential has a minimum energy of -3.05 eV at r = 1.5 Å, which is a good representation of the Si-H bond-energy and bond-length in a-Si:H. In addition, the potential leads to the H-Si stretching mode frequency of 2023 cm^{-1} in good agreement with experimental values in a-Si:H. The cut-off function $g_c(r)$ was designed to ensure the short range nature of the interaction using a simple smooth functional form.

A three-body potential is essential for modeling the covalent Si-H interaction and for stabilizing the tetrahedral environment of Si. We have developed a three-body potential for Si-H interactions, similar to Si-Si interatomic potential [30], which is

$$V_3(r_{12}, r_{13}, \theta) = B_H \phi_{1,2}(r_{12})\phi_2(r_{13})(\cos\theta + \frac{1}{3})^2 h_{c_{1,2}}(r_{12}) h_{c_2}(r_{13})\,, \tag{3.3}$$

where the subscripts 1 and 2 refer to Si-Si and Si-H interactions, respectively [67]. As in previous work [30], we use a Keating form for the angular dependence of the potential. Here, $\phi_1(r) = \exp(-\alpha r^2)$ and $\phi_2(r) = \exp(-\alpha_H r^2)$ are radial functions and $h_{c_{1,2}}(r) = [1 + \exp(\frac{r - r_{c_{1,2}}}{\mu_{1,2}})]^{-1}$ is a cut-off function. We adopt the same form of the cut-off function $f_c(r)$ as used in previous work [30], except for new parameters (r_{c_2} and μ_2) for the Si-H interaction to ensure the shorter range nature of the interaction. The parameters of the potential B_H and α_H were obtained by fitting to the H-Si wagging mode of 630 cm^{-1} and the scissors bending mode of 897 cm^{-1} in a-Si:H. This three-body potential describes Si-Si-H, H-Si-H, or even Si-H-Si interactions, and its strength ensures that the lowest energy configuration of a H atom is when the H atom is bonded to a single Si atom.

In conjunction with this Si-H model, we have used the Biswas-Hamann two- and three-body interatomic potentials for Si-Si interactions [30], which have had much success in describing several properties of pure a-Si and Si thin film growth [22, 60].

We have also used a repulsive H-H interatomic potential V_2^{H-H}, similar to that employed by Mousseau and Lewis [64], that prevents H atoms from approaching unphysically close to each other, where [68]

$$V_2^{H-H}(r) = (\frac{\epsilon}{1 - \frac{6}{\alpha_{HH}}})\{\frac{6}{\alpha_{HH}} \exp[\alpha_{HH}(1 - \frac{r}{\sigma})] - (\frac{\sigma}{r})^6\} \qquad (3.4)$$

Therefore, H_2 molecular formation is inhibited in this scheme, but that is less important for the purposes of this paper. Clearly, an extension of this model would be to incorporate a H-H molecular potential.

In our model, all Si-H interactions are described through equations (3.1 - 3.3). In contrast to this model, we note that Guttman and Fong [69] used a Keating potential

for bonded Si-H pairs and a repulsive potential of the form $(r_{Si-H})^{-6}$ between H and Si atoms that were not bonded to each other in constructing a-Si:H models. Although a Keating potential can also gives a good description of the vibrational properties of a-Si:H [61], it is not sufficient for molecular dynamics simulations.

Structure of Hydrogenated Amorphous Silicon

In our approach to structural modeling of a-Si:H, we started with a-Si:H networks proposed by Guttman and Fong [69]. In their scheme, a pair of H atoms were introduced to a four-coordinated pure a-Si network. Their approach consisted of by first making a new bond between two Si atoms that were close but unbonded, breaking some other bond to each, and attaching H atoms to the two remaining dangling bonds. Hence, two Si-H bonds in monohydride bonding species were introduced with the two H atoms more spatially separated than if they were attached to a bonded pair of Si atoms. The procedure to make dihydride bonding groups was to break two bonds on a Si atom, attach two H atoms there, and then make a new bond between the two remaining Si atoms that had dangling bonds. They used Keating-type potentials to relax the a-Si:H structures.

We have relaxed a monohydride-containing a-Si:H network which contains 60 atoms with 54 Si atoms and 6 H atoms, i.e., containing 10 at.% H, with our Si-H interatomic potential together with the Biswas-Hamann Si-Si interatomic potential [30]. Our repulsive H-H interatomic potential was also used for H-H interactions. Periodic boundary conditions were used in a cubic cell to avoid spurious surface effects. The density of the system was allowed to vary to find the minimum energy configuration. The most relaxed configuration (*MH1*) has a mass density about 8

% smaller than the crystalline Si density. An appealing feature of the model is the absence of dangling-bond or floating-bond defects. A bond cutoff of 3.0 Å and of 1.7 Å were used to define Si-Si bonds and Si-H bonds, respectively. All H atoms remain in monohydride form and the average Si-H bond-length is 1.55 Å which is slightly larger than the experimental value 1.48 Å. The Si-Si bonds have a distribution of bond-lengths with an rms value of 0.10 Å, whereas the Si-H bonds have an extremely narrow distribution of bond-lengths with an rms value of 0.01 Å.

The Si-Si partial pair correlation function $g_{Si-Si}(r)$ for the *MH1* (Figure 3.1) is comparable to the experimental measurement [70] except for the slight mismatch of the peak positions. The difference comes from the larger Si-Si equilibrium bond-length (2.50 Å) caused by strengthening the three-body Si-Si potential which was necessary for the satisfactory description of a-Si [22]. Figure 3.2 shows the Si-H partial pair correlation function $g_{Si-H}(r)$ together with the experimental result [70]. The agreement is remarkable except that the first peak is much sharper than the experimental result. The experimental curve involves subtraction of structure factor measurements of a-Si:H from a different a-Si sample, a procedure that also introduces uncertainties. The peak around r = 3.2 Å corresponds to the distances between H atoms and the nearest Si neighbors of the monohydride Si atoms.

The bond-angle distributions for the *MH1* is given in Figure 3.3. The rms bond-angle deviation of the network is 10.4°, which is smaller than 11° - 14° of typical computer-generated pure a-Si networks [20, 21, 22, 23]. Also, there is no tail below 80° or above 150° in contrast to pure a-Si networks. The introduction of H into the a-Si networks substantially reduces the local strain of the system, as is known in experimental studies.

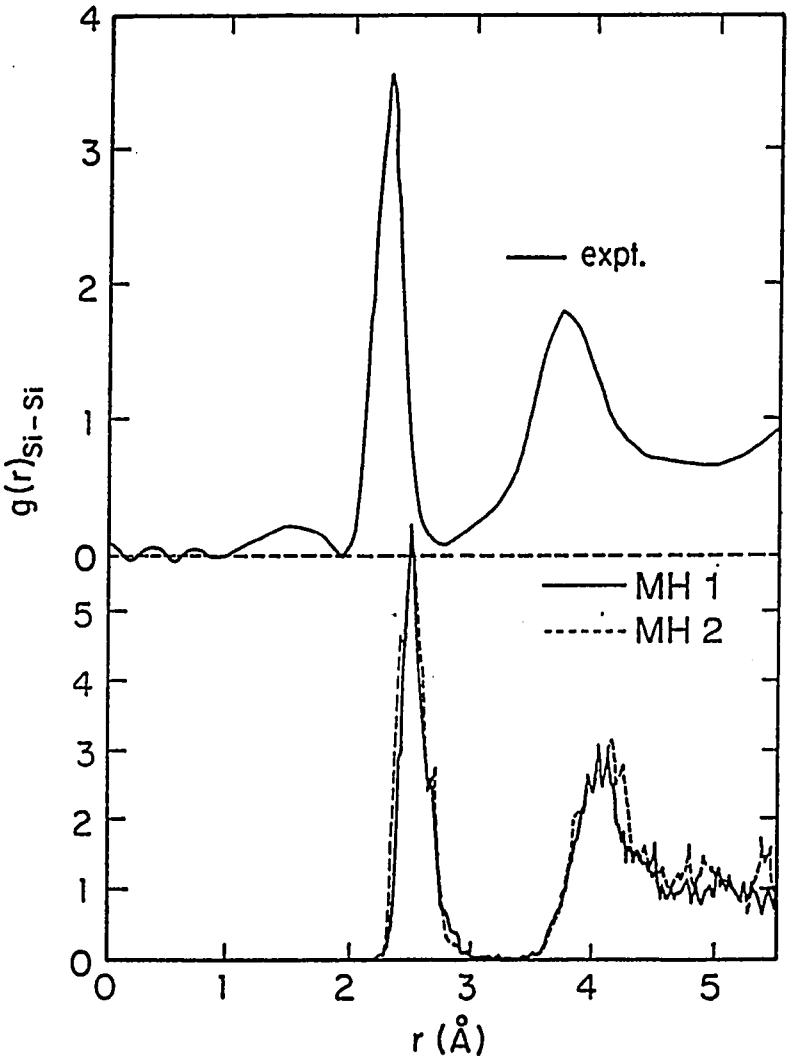

Figure 3.1: Si-Si partial pair correlation function $g_{Si-Si}(r)$ for a-Si:H models (*MH1* and *MH2*), compared to the experimental data of Bellisent et al. [70]

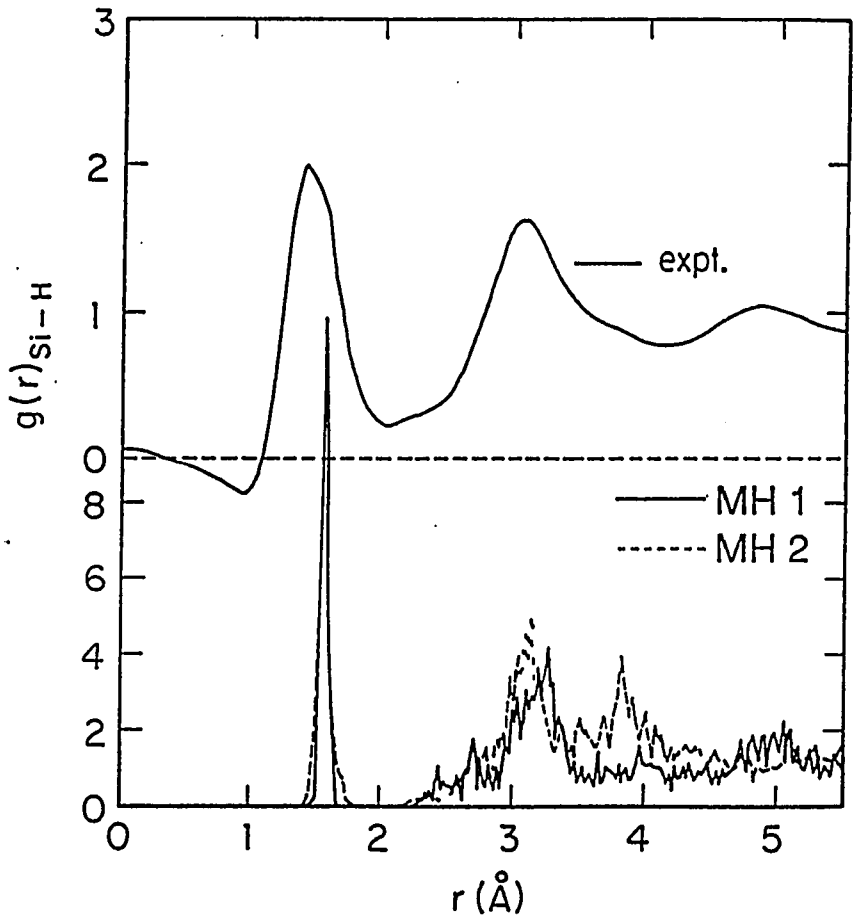

Figure 3.2: Si-H partial pair correlation function $g_{Si-H}(r)$ for a-Si:H models (*MH1* and *MH2*), compared to the experimental data of Bellisent et al. [70]

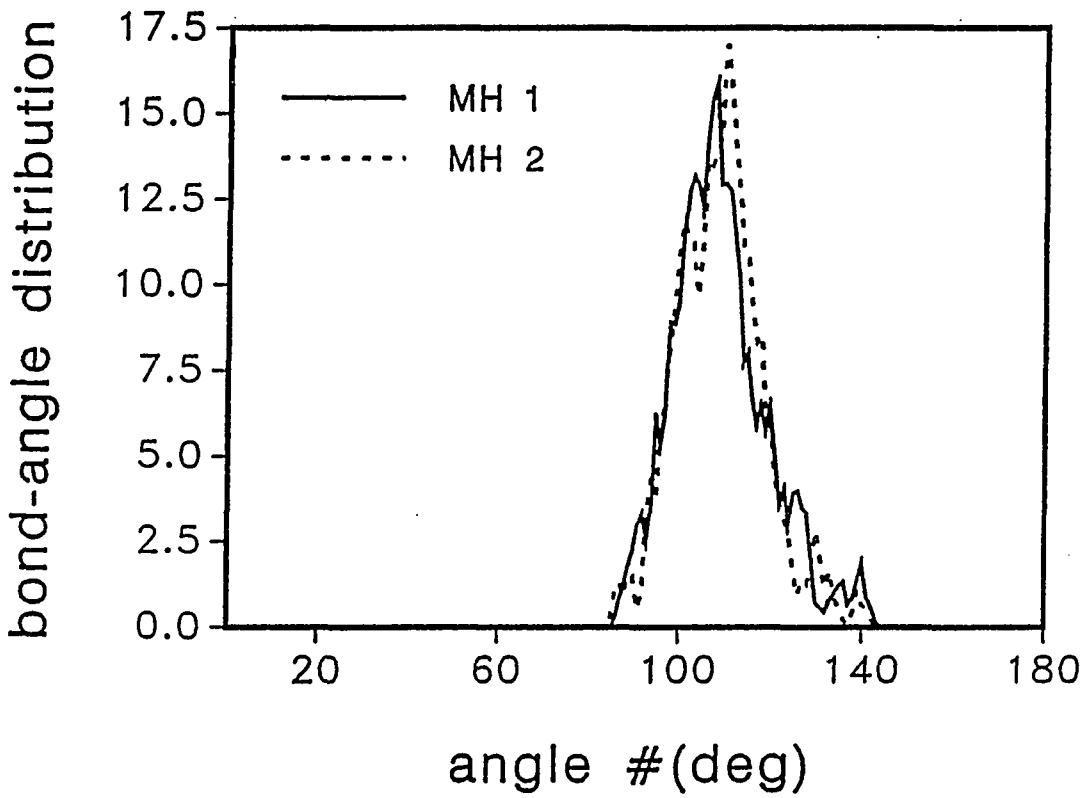

Figure 3.3: Bond-angle distributions for a-Si:H models (*MH1* and *MH2*)

We have developed another network model of a-Si:H, which has dihydride bonding species, to study further the role of H atoms and to compare stability properties of monohydride and dihydride bonding species. This system consists of 54 Si atoms and 14 H atoms with 3 dihydrides and 8 monohydrides, i.e., 20.6 at.% H in the network. We first started with the network developed by Guttman and Fong [69] which had 54 Si atoms and 3 dihydrides (6 H atoms). When we relaxed this network with our potential, there were 8 dangling-bond defects. Thus, 8 H atoms were added to saturate dangling bonds and the system was relaxed further with variations of the density.

It is highly desirable to have coordination defect-free configurations for molecular dynamics simulations of the light-induced defect formation process which will be discussed in Chapter 4. This is necessary so that light-induced (i.e., in the structure excitation-induced) defects can be clearly distinguished from the initial defects. Also, device-quality a-Si:H films with defect densities of an order of 10^{15} cm^{-3} may be best modeled by defect-free finite size networks.

The most relaxed configuration (*MH2*) with the density about 10 % smaller than the crystalline Si density has no coordination defects with a bond cut-off of 3.10 Å for Si-Si bonds and 1.7 Å for Si-H bonds. The rms bond-length deviation is 0.13 Å for Si-Si bonds, and 0.03 Å for Si-H bonds. The partial pair correlation functions of the *MH2* are very similar to those of the *MH1* (Figure 3.1 and 3.2). However, the rms bond-angle deviation of the *MH2* is 9.51° which is smaller than 10.4° of the *MH1*. The increase of H content from 10 at.% of the *MH1* to 20.6 at.% of the *MH2* causes the decrease of the bond-angle distortions.

One important difference between the *MH1* and the *MH2*, that is not quite

apparent in Figure 3.1, is a substantial increase in the number of weak Si-Si bonds in the *MH2*. This may reflect the lower network stability or the less desirable features of dihydride bonding species. Alternatively, this may be due to the way in which the a-Si:H network was initially generated.

CHAPTER 4. THE STAEBLER-WRONSKI EFFECT IN HYDROGENATED AMORPHOUS SILICON

The understanding of the Staebler-Wronski effect [5], the light-induced degradation of hydrogenated amorphous silicon (a-Si:H), is essential for both basic science and solar energy conversion applications. In the Staebler-Wronski effect, exposure of a-Si:H to light causes an increase in the density of metastable defect states in the gap region that can be removed by thermal annealing at 150° - 200° C [7]. The metastable defects are paramagnetic and are commonly believed to be Si dangling bonds. Prolonged illumination, particularly at high intensities of light, leads to a saturation of the metastable defect density with saturated densities of an order of 10^{17} cm^{-3} for device-quality films [71]. Around room temperature, the saturated metastable defect density is independent of light intensity, and is found to correlate with the hydrogen content and the optical band gap [72].

Despite extensive studies, the microscopic mechanisms for the Staebler-Wronski effect remain unclear. Several different mechanisms have been proposed for the Staebler-Wronski effect. The mechanisms, intrinsic to a-Si:H, include the breaking of weak Si-Si bonds by non-radiative recombination of photo-excited carriers and the creation of metastable dangling bonds [7, 8, 9, 10], the capture of carriers at existing charged dangling-bond sites resulting in paramagnetic neutral dangling-bond

defects [8, 11], the generation of pairs of dangling-bond and floating-bond defects [12]. Another class of intrinsic mechanisms that has received much attention recently involves hydrogen-induced defects and includes the formation of metastable diatomic H-complexes in a-Si:H [13, 14] and the role of H-interstitials [15]. The mechanisms, extrinsic to a-Si:H, include a recent model for the metastable states of dopant atoms in a-Si:H and suggestions that impurity atoms may be responsible for light-induced degradation [16].

Among these various models, the bond-breaking model has received a great deal of attention. In this model, the energy released by recombination of photo-excited electron-hole pairs leads to breaking of weak Si-Si bonds. Stutzmann, Jackson, and Tsai [7] proposed that the weak Si-Si bond would be a back bond of an monohydride site and that hydrogen is then involved in the microscopic mechanism as a stabilizing element. Rupture of this weak Si-Si bond is followed by reorientation of the H into the broken bond location leading to two dangling bonds that are pointed away from each other and are therefore paramagnetic. Although some experimental measurements could not be explained by the bond-breaking model, it is the most generally accepted model for the Staebler-Wronski effect.

A difficulty in many of the previous studies was the lack of a realistic atomic model of a-Si:H. In this chapter, we overcome this difficulty by describing a new molecular dynamics approach that can directly deal with realistic atomic structural models of a-Si:H. The molecular dynamics approach offers great promise in investigating the mechanisms of light-induced degradation and the various models of the proposed light-induced defects.

Hot Spot Model in Amorphous Silicon

In this section, as a first step toward understanding mechanisms for the Staebler-Wronski effect, we will focus on models of amorphous silicon that do not contain H, and anticipate that the present results will guide future work with hydrogenated amorphous silicon models. We discuss three classes of models: (i) the four-coordinated WWW model, (ii) an a-Si model with a substantial density of overcoordinated defects, and (iii) crystalline silicon. Molecular dynamics simulations were performed with the Stillinger-Weber potential [28]. This potential involves both a two- and three-body term,

$$\Phi = \sum_{i<j} v_2(i,j) + \sum_{i<j<k} v_3(i,j,k), \tag{4.1}$$

where i, j, and k are particle labels and

$$v_2(r_{ij}) = \varepsilon f_2(\frac{r_{ij}}{\sigma}) \tag{4.2}$$

$$v_3(\vec{r}_i,\vec{r}_j,\vec{r}_k) = \varepsilon f_3(\frac{|\vec{r}_i-\vec{r}_j|}{\sigma},\frac{|\vec{r}_j-\vec{r}_k|}{\sigma},\frac{|\vec{r}_k-\vec{r}_i|}{\sigma}). \tag{4.3}$$

Here, ε in energy units is chosen to give f_2 a depth of -1 and σ in length units is chosen to make $f_2(2^{1/6})$ vanish. This being done, all lengths and energies are hereafter dimensionless. The explicit form of the pair potential as a function of this dimensionless coordinate is

$$f_2(r) = \begin{cases} A(Br^{-p} - r^{-q})\exp(\frac{1}{r-a}), & r < a \\ 0, & r \geq a \end{cases} \tag{4.4}$$

where A, B, p, and a are all positive. This function and all of its derivatives are continuous at the cutoff $r = a$. The three-body interaction is composed of three

terms,

$$f_3(\frac{|\vec{r}_i - \vec{r}_j|}{\sigma}, \frac{|\vec{r}_y - \vec{r}_k|}{\sigma}, \frac{|\vec{r}_k - \vec{r}_i|}{\sigma}) =$$
$$h(r_{ij}, r_{ik}, \theta_{jik}) + h(r_{ji}, r_{jk}, \theta_{ijk}) + h(r_{ki}, r_{kj}, \theta_{ikj}), \qquad (4.5)$$

where θ_{jik} is the angle between $\vec{r}_j$ and $\vec{r}_k$ subtended at vertex i, etc. The function h has the form

$$h(r_{ij}, r_{ik}, \theta_{jik}) = \begin{cases} \lambda \exp(\frac{\gamma}{r_{ij}-a} + \frac{\gamma}{r_{ik}-a})(\cos\theta_{jik} + \frac{1}{3})^2 & \text{for } r_{ij} < a \text{ and } r_{ik} < a \\ 0 & \text{otherwise,} \end{cases} \qquad (4.6)$$

where both λ and γ are greater than zero and the function and all its derivatives are continuous at the cutoff at $r = a$. The ideal tetrahedral angle appropriate for the silicon crystal structure is favored by the $(\cos\theta_{jik} + \frac{1}{3})^2$ term. The parameters in the Stillinger-Weber potential were chosen so as to make the diamond structure the most stable periodic arrangement of atoms at low pressure [73]. The result presented here may also be relevant for annealing phenomena and understanding the differences between a-Si models developed under different theoretical preparation methods.

Metastable mid-gap defects are produced either by illumination or by excess carrier injection in a-Si:H. Hence, it is commonly believed that the non-radiative recombination of photo-excited carriers is responsible for the creation of metastable defects in a-Si:H under illumination. The transfer of the recombination energy of an excited electron-hole pair to the system is a difficult problem involving the electron-phonon interaction. A simple and computationally feasible way to model the energy transfer is to assume that the non-radiative recombination event creates a local "hot spot" or a local region of a few excited atoms in the network [74]. We expect this non-radiative decay channel to be much weaker than the dominant radiative decay

channel. In fact, Weeks, Tully, and Kimmerling [75] have argued that the non-radiative carrier-recombination energy can be largely converted into the vibrational energy that is localized in the vicinity of a defect.

In the molecular dynamics simulations, we create a hot spot by providing an excess kinetic energy to a local region and allow the system to dynamically evolve and equilibrate. Typical equilibration times are 5000 - 7000 time steps (18.5 - 25.9 ps). One time step corresponds to 0.0037 ps. Velocities of atoms in the hot spot can be either in random directions, or along the bond, or perpendicular to the bond. We examine whether the local excitation can lead to structural changes or defects. A convenient way to study resulting structural changes is performing a steepest descent relaxation on the equilibrated configuration. The steepest descent relaxation gives the intrinsic configuration and separates the thermal disorder from the underlying structural disorder. The variables we have studied in the dynamical simulations are (i) the extent of the locally excited region, (ii) the spatial locations of hot spots, and (iii) the amount of excitation energies. A simple approach to (i) is to provide excess energy to a single bond, i.e., two bonded atoms, as opposed to an extended atomic cluster.

We first tested our approach with crystalline silicon (c-Si). Local excitations of energy 1.7 - 8.0 eV in c-Si failed to induce structural changes. This is consistent with the Frenkel pair energy for a vacancy-interstitial pair being 8.0 eV in c-Si, and involving an even larger energy barrier for structural changes. The perfect crystal without any impurities or defects would then not show light-induced structural changes. In contrast, the energy surface of a-Si has a number of nearby local minima separated by small energy barriers, and hence structural changes are much more readily induced,

as discussed below.

We first consider the WWW model, which was relaxed at zero temperature to a local minimum with the Stillinger-Weber potential. The WWW model has 216 atoms with periodic boundary conditions. The WWW model may be a realistic representation of a defect-free region of an experimental a-Si film. The most significant result is that structural changes are very spatially dependent on the location of the hot spot. Choosing an excitation region at random usually leads to equilibration and no structural changes. We have identified two local regions of the WWW networks where excitation-induced structural changes are possible. Both of these local regions involve weak Si-Si bonds or weakly bonded Si sites.

The first region [Figure 4.1(a)] involves a weak bond (R = 2.53 Å, where the mean bond length is 2.35 Å) between two atoms one of which (atom 126) is the most weakly bound site in the model with a site energy $E_S = -3.30$ eV, substantially higher than the average site energy of -4.07 eV for the WWW model ($E_S = -4.33$ eV for the crystal). The bond-angles and bond-lengths are highly strained on this atom. Creation of a hot spot on this bond and equilibration broke the 122-126 bond creating two dangling bonds on these sites [Figure 4.1(a)]. Some shearing motion of this bond is also involved. Resulting atomic displacements are shown in Figure 4.2(a). This bond-breaking process requires an excitation-energy threshold of about 1.0 eV, and no changes are observed with a lower energy of 0.4 eV. The energy for the broken-bond configuration was only 0.14 eV higher than the initial state. The structural change decreases the bond-angle and bond-length distortions (Figure 4.2) on these sites (122, 126) which are now more than 3.0 Å apart. To accommodate this local strain relief, atoms in the vicinity of these two sites have sizable displacements,

[0.1 - 0.4 Å, Figure 4.2(a)] and an overall increase in the strains of these atoms. We have performed electronic structure calculations with the Chadi model [76] which confirm that the final configuration does have two localized gap states, primarily localized on each dangling bond, that would give ESR signals. In each of these states there is a mixing of 7 % and 4 % of the wave function of the other nearby dangling bond.

The time scales of our molecular dynamics simulation are limited to being between 10 ps and 100 ps. Over substantially longer times, it may be possible for one of these dangling bonds to diffuse away from the local region of Figure 4.1(a), resulting in isolated dangling bond defects. Annealing at 300 - 330 K rebonded the 122-126 atom pair illustrating the metastability of this configuration. The annealing did however lead to extra floating bonds in the region away from this defect center. We feel that these floating bond defects are an artifact of the present Si-model, which may unphysically favor overcoordinated configurations. The bond-breaking change could not be produced by more extended cluster excitations (5 atoms around 126), or exciting different bonds on 126, and 122.

The second site [Figure 4.1(b)] involves breaking a weak bond on one site (atom 58) and formation of a new bond between 58 and 57, leading to a pair of nearby dangling and floating bonds and an energy lowering of 0.8 eV. This change can also be induced by excitations of as low as 0.4 eV, on a number of different sites spatially separated from this region. The floating bond does not migrate over time scales of 40 ps, although longer time behaviour is hard to infer with the molecular dynamics simulation. The formation of a similar pair of dangling and floating bonds was proposed by Pantelides [12] to be a fundamental defect reaction underlying the light-

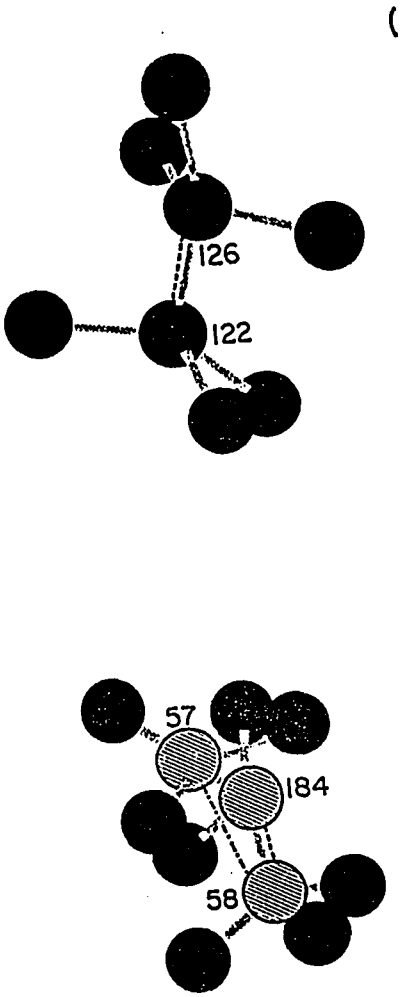

Figure 4.1: (a) Defect center involving a weak Si-Si bond between atoms 122 and 126 (dashed line), which is broken after the local excitation process. Atom 126 is very weakly bound with a site energy of −3.30 eV. (b) A metastable configuration that can be altered on excitation, by creation of a new bond between 58 and 57 (dot-dashed line) and elimination of the bond between 58 and 184 (dashed line)

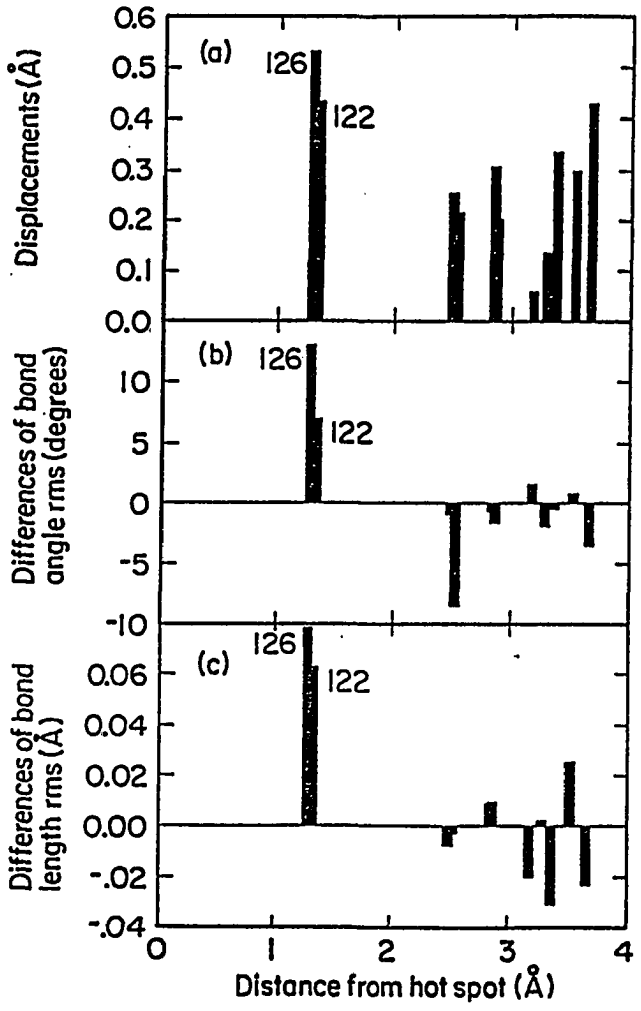

Figure 4.2: Structural changes after local excitation in the region in Figure 4.1(a) illustrated by (a) atomic displacements, (b) changes in bond angle distributions and (c) changes in bond length distributions on atoms around excitation region. Plotted in (b) and (c) are differences between initial and final values so that positive bars indicate a relaxation and negative bars, an increase of the strain. Distances are from the center of the 122-126 bond

induced degradation. It was proposed [4, 12] that the floating bonds could migrate, leaving isolated defects, whereas annealing would require defect reactions with H. We however found that this structural change could also be thermally induced by heating the sample to 300 - 350 K, suggesting that this change is due to a poorly relaxed local region of the original network, unrelated to degradation processes.

The above results indicate a limited number of atomic sites at which structural degradation changes are possible, a concept suggested by the observed saturation of the light-induced defect density in a-Si:H [71, 72]. These results are independent of the method of preparation of a-Si and the Si potential used. Simulations of a melt-quenched a-Si model (generated by Biswas, Grest and Soukoulis [22] utilizing a different Si-potential, the Biswas-Hamann model [30]) showed similar results for breaking of weak bonds and a threshold energy of 1.0 eV for excitation-induced structural changes. The bond breaking process was also very spatially dependent affecting weakly bonded Si-sites. Similar behaviour is also observed at higher temperature. Local excitations of the WWW model at 325 K and 590 K also resulted in breaking of weak bonds, with decrease of energy thresholds and larger number of defects with increasing temperatures.

Further multiple local excitations in the vicinity of the site in Figure 4.1(a) increased the number of coordination defects, accompanied by an energy lowering of the network, suggesting an annealing of the structure. To systematically examine the stability of the WWW model, we thermally annealed the WWW model by equilibrating it at various temperatures up to 1250 K. We then performed steepest descent quenches at various temperatures to extract inherent structures, free from thermal disorder. The potential energy of these inherent structures (Figure 4.3) is minimized

for the 1040 K anneal temperature, and then rises as the amorphous-liquid transition is approached. This transition temperature was determined by Luedtke and Landman (LL) [23] to be 1435 K for rapid heating and about 1082 K for slow heating. The WWW model although a local minimum of this Si-potential [28], can thus be annealed further by 0.03 eV/atom. The steepest descent configuration from the 1040 K anneal was equilibrated near room temperature (313 K) and had a radial distribution function (Figure 4.3) very similar to the slow-cooled a-Si obtained by Luedtke and Landman [23] (also at 300 K) including the weak shoulder at 3.2 Å, but unlike the glass obtained by Luedtke and Landman which had a distinct peak at 3.2 Å. Our 216-atom configuration was substantially overcoordinated with 27.8 % five- and 1.9 % six-coordinated atoms, and no dangling bonds, for the T = 0 network (or 30.5 % and 2.3 % at 313 K), using a bond cutoff of 2.95 Å. These defect densities are closer to the densities of overcoordinated defect densities in the LL a-Si model (21 %), than the LL glass (59 %).

Our third class of simulations involved the above annealed overcoordinated a-Si model. In all cases, local 1.7 eV excitations on bonds led to a new metastable configuration with a somewhat higher energy (0.01 - 0.06 eV for 216 atoms) than the starting configuration, accompanied by an increase in the number of overcoordinated defects. The starting configuration is a stable local minimum. This is consistent with previous results for the WWW model where hot spots also lead to an increase in the number of defects.

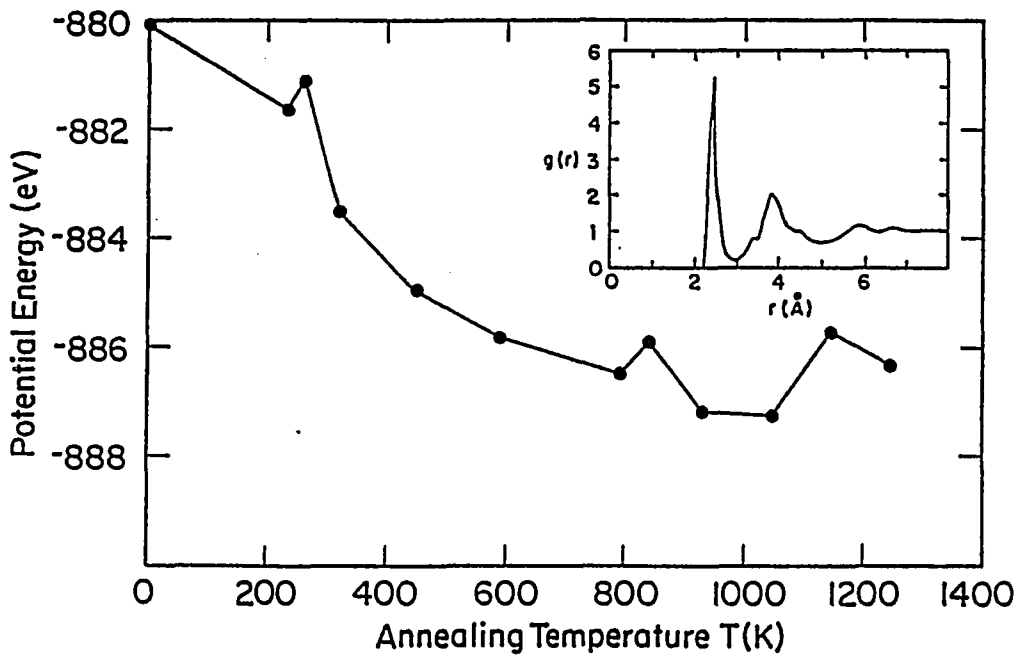

Figure 4.3: Potential energies of inherent a-Si models as a function of anneal temperature. The steepest descent quenched a-Si model from the 1040 K anneal was equilibrated near room temperature to produce the pair correlation function $g(r)$ in the inset

Bond-Breaking Model of the Staebler-Wronski Effect

In this section, we examine the bond-breaking model for the Staebler-Wronski effect with simulations of local excitations in atomic structural models of a-Si:H developed in Chapter 3. A localized hot spot has been used to model the non-radiative energy transfer of photo-excited carriers to the system by providing an excess kinetic energy to two bonded atoms. The system then was allowed to dynamically evolve and equilibrate. Velocities of atoms can be either in random directions or along the bond. In the molecular dynamics simulations, the new classical interatomic potential for Si-H interactions described in Chapter 3 was employed, in conjunction with the Biswas-Hamann potential model [30] for Si-Si interactions. The repulsive H-H interatomic potential described in Chapter 3 was also used to prevent H atoms from approaching unphysically close to each other. We examine whether the local excitation can lead to structural changes or defects. Defect formation and annealing are discussed with their dependences on hot spot location, hydrogenation of Si, and amount of energy transfer.

We first note that the *MH1* containing monohydrides is very stable to thermal annealing up to 700 K, and no lower energy configuration could be produced by quenching or cooling from elevated temperatures. Hence, this a-Si:H model with no coordination defects is a good starting configuration for the investigations of the Staebler-Wronski effect.

To examine the bond-breaking mechanism suggested by Stutzmann et al. [7], we first tested Si-Si bonds on monohydride sites in the network of the *MH1*. We have applied hot spots on Si-Si bonds 40-41, 42-48, 42-43, and 42-7 (Table 4.1). 40 and 42 are monohydride sites and the bond-lengths of these bonds are longer than other Si-Si

bonds on monohydride sites. Excitations of 1.7 eV (i.e., an excess kinetic energy of 0.85 eV to each atom) on various Si-Si bonds did not produce any structural change after dynamical evolution of 50,000 time steps (9.25 ps) in all cases. Figure 4.4(a) is the kinetic energy per atom in the vicinity of the hot spot of the 40-41 pair as a function of time and shows how the system equilibrates. After the local excitation, the excess kinetic energies of the atoms 40 and 41 dissipate to the rest of the system. The information on structural changes induced by the hot spot excitation is obtained by plotting the bond-length of the excited Si-Si pair and the distances of the H from each of these atoms [Figure 4.4(b)]. Bond-lengths of these three atom pairs fluctuated only by a small amount, resulting in no defect creation. Simulations were done at room temperature and led to similar results, with the structure essentially returning to its initial configuration after equilibration of the excess energy.

One hypothesis we investigated was that the bond-breaking process may be a low probability event so that it may not be observed with a finite number of simulations. To increase the probability of such a bond-breaking process, we increased the excitation energy to as large as 7.0 eV (Table 4.1), far in excess of the possible recombination energy or the optical gap. In spite of the larger energy 3.0 eV to 7.0 eV excitations, we did not observe any process where dangling bonds or other coordination defects were produced, except for the 19-29 case (at 3.0 eV), and the model returned to its initial configuration. We note that the breaking of the bond 19-29 was seen by thermal activation by equilibration above 700 K. Therefore, the breaking of the bond 19-29 with a hot spot excitation of 3.0 eV is not related to the light-induced degradation process in a-Si:H.

To study the effect of the finite size of the system, we constructed a system of

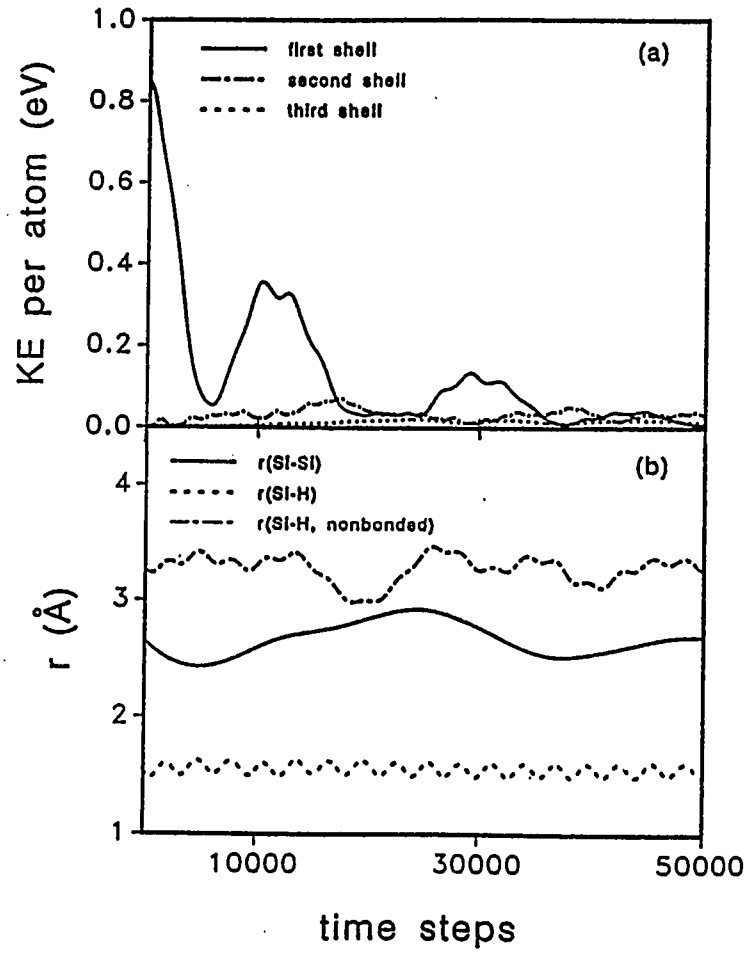

Figure 4.4: (a) Kinetic energy per atom as a function of time, when a hot spot with excitation energy of 1.7 eV was given to atoms 40 and 41 in the *MH1*. The directions of the velocities were random. The first shell is the hot spot atoms 40 and 41, the second shell is the 6 nearest neighbor atoms of 40 and 41, and the third shell the second nearest neighbor atoms. (b) Distances between the excited atoms 40 and 41 r(Si-Si), between the hot spot atom 40 and its bonded neighboring H atom r(Si-H), and the distance between the other hot spot atom 41 and the H atom, which is bonded to 40, r(Si-H, non-bonded), as a function of time. One time step corresponds to 0.185 fs

Table 4.1: Hot spot excitations on the model *MH1* which has 10 at.% H with 6 monohydrides only. One time step corresponds to 0.185 fs

site	r(Å)	energy(eV)	direction	time steps	result
19-29	2.917	1.7	random	30,000	no change
		2.5	random	30,000	no change
		3.0	random	30,000	no change
		3.0	bond	110,000	19-29 broken
34-51	2.701	1.7	random	30,000	no change
		3.0	random	30,000	no change
		3.0	bond	50,000	no change
		4.0	bond	50,000	no change
		5.0	bond	50,000	no change
		7.0	bond	50,000	no change
42-48	2.682	1.7	random	50,000	no change
40-41	2.656	1.7	random	50,000	no change
		3.0	random	50,000	no change
40-57	1.541	1.7	random	50,000	no change
		3.0	random	30,000	no change
at room	temperature:				
42-7	2.665	1.7	random	50,000	no change
42-43	2.602	1.7	random	50,000	no change
42-58	1.550	1.7	random	50,000	no change

480 atoms by combining together 8 of the 60-atom cells. Excitations on this enlarged system gave a similar result for the stability to local excitations. We conclude that the a-Si:H network, *MH1*, with 10 at.% H and no coordination defects, similar to device-quality a-Si:H materials, is very stable to local excitations.

We next examined the stability of the model containing dihydride bonding species to local excitations. In the a-Si:H network, *MH2*, with 20.6 at.% H and dihydride bonding species, there were two cases of structural changes induced by hot spot excitations (Table 4.2). In the first case, atoms 49 and 50, which have higher site energies than other atoms, were excited in the bond direction with 1.7 eV excitation, resulting in the bond being broken. Both atoms were more than 4.2 Å apart after dynamical evolution of 70,000 time steps (12.95 ps) (Figure 4.5). This time is sufficient for the equilibration of the system, as verified by the energy relaxation plot that is similar to Figure 4.4(a).

Here, the site energy of an atom is defined in such a way that two-body potential is divided to each atom which is bonded to each other and three-body potential is given to the vertex atom. Both 49 and 50 have very large bond-angle distortions, resulting in high site energies.

There are additional structural changes in the vicinity of the 49-50 pair induced by the hot spot excitation. Two neighboring bonds (13-52 and 32-54) are broken and a new bond between 50 and 52 is formed. Therefore, there are four dangling bonds in the final configuration [Figure 4.6(a)]. The energy of the final configuration after a steepest descent relaxation is 0.64 eV (ΔE) higher than the energy of the initial configuration [Figure 4.6(b)].

We have calculated electronic densities of states of both the initial configuration

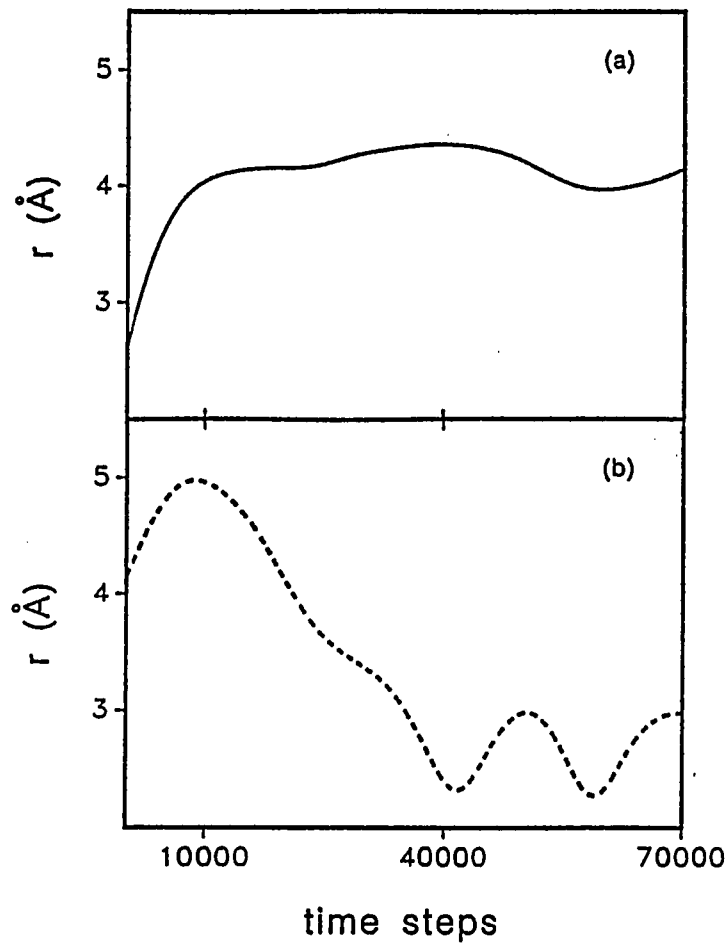

Figure 4.5: (a) Distance between 49 and 50 in the *MH2* as a function of time. A hot spot excitation energy of 1.7 eV was given along the bond direction. (b) Distance between 49 and 50 as a function of time, when the system was thermally annealed at about 560 K after the hot spot excitation

Table 4.2: Hot spot excitations on the model *MH2* which has 20.6 at.% H with 8 monohydrides and 3 dihydrides. One time step corresponds to 0.185 fs

site	r(Å)	energy(eV)	direction	time steps	result
32-54	2.875	1.7	random	50,000	no change
		1.7	bond	70,000	no change
49-50	2.610	1.7	random	30,000	no change
		1.7	bond	90,000	49-50 broken
		1.2	bond	50,000	no change
53-54	2.407	1.7	bond	30,000	no change
19-32	2.461	1.7	random	50,000	no change
		1.7	bond	50,000	no change
		3.0	bond	110,000	no change
23-56	1.610	1.7	random	30,000	no change
		1.7	bond	50,000	no change
34-57	1.527	1.7	bond	30,000	no change
34-58	1.535	1.7	bond	50,000	no change
38-66	1.538	1.7	bond	30,000	no change
at room	temperature:				
32-54	2.875	1.7	bond	70,000	32-54 broken
19-32	2.461	1.7	random	70,000	no change
		1.7	bond	70,000	no change
34-57	1.527	1.7	bond	50,000	no change
38-66	1.538	1.7	bond	30,000	no change

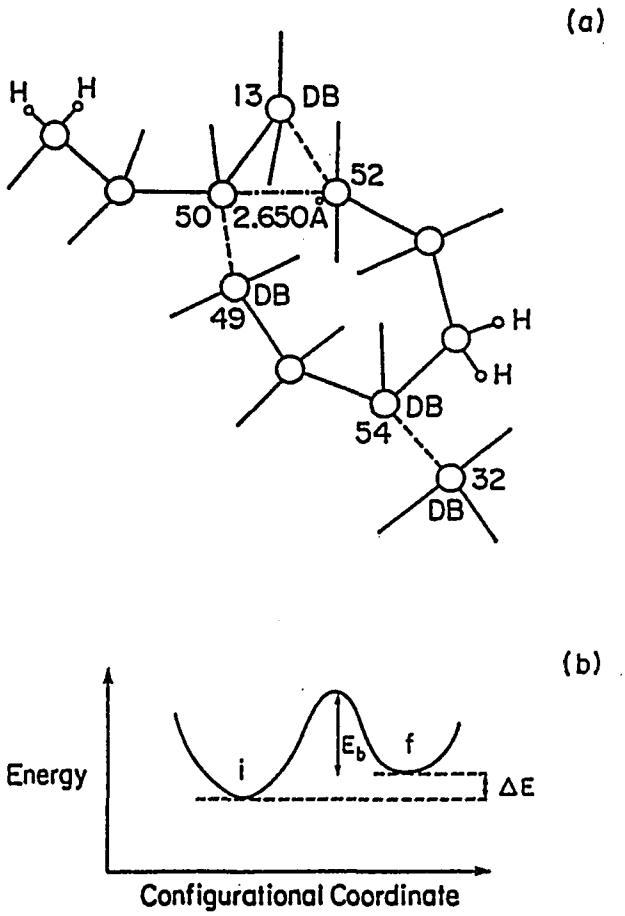

Figure 4.6: (a) Atomic configuration in the vicinity of the 49-50 pair after the hot spot excitation of 1.7 eV on the pair. The bonds 49-50, 32-54, and 13-52 are broken (dashed line), and a new bond between 50 and 52 is formed (dot-dashed line), resulting 4 dangling bonds (DB) in the network. (b) Schematic energy level diagram for the two configurations, before the hot spot excitation (i) and after (f)

and the final configuration using an empirical tight binding method. For the Si-H interaction, we have used the tight binding parameters obtained by Min et al. [77] by fitting to vibrational frequencies of SiH_4. These parameters describe quantitatively well the electronic properties and the vibrational properties of the hydrogenated Si(111) surface. The Chadi parameters [76] were used for Si-Si interactions. Figure 4.7 shows that the initial configuration with no dangling bonds has a well-defined gap of about 1.3 eV, whereas the higher energy configuration has gap states induced by dangling bonds.

We investigated the stability of the higher energy configuration by thermally annealing the final configuration. Annealing in the temperature range from 270 K to 560 K relaxed the structure back to its original configuration after 40,000 time steps, as illustrated by Figure 4.5(b), where the bond between 49 and 50 reforms and then fluctuates about its initial distance 2.61 Å. This annealing kinetics indicates a small energy barrier E_b of about 0.11 eV separating this higher energy configuration from the initial configuration. The higher energy configuration is then only weakly stable and the annealing energy barrier is smaller than that expected for light induced defects (0.9 - 1.3 eV) [7].

The second example of defect formation by hot spot excitations is the 32-54 pair. The bond-length of the 32-54 pair, 2.875 Å, is longer than the average bond-length, 2.541 Å, and both atoms have higher site energies. At room temperature, the bond 32-54 was broken by an excitation of 1.7 eV, although no change was observed when the excitation was applied to the zero temperature configuration. The energy of the final configuration after a steepest descent relaxation is 0.15 eV higher than the energy of the initial configuration, and the higher energy configuration has two dangling

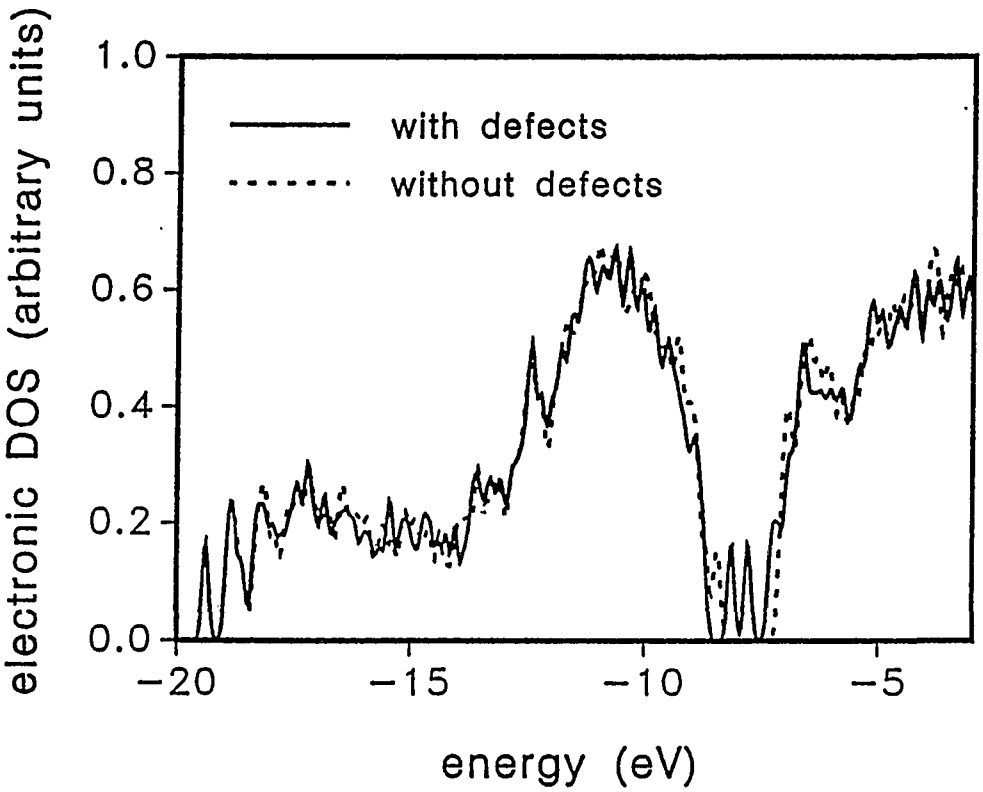

Figure 4.7: Electronic density of states for the initial configuration of the *MH2* (without defects) and for the configuration after excitation of atoms 49 and 50 (with defects), using the empirical tight binding method

bonds (on 32 and 54). This higher energy configuration could be easily annealed back to the initial configuration at room temperature in 20,000 time steps - implying only a very small barrier of about 0.04 eV separating it from the initial state. This higher energy configuration may in fact be a transient state rather than a metastable state. As seen in the *MH1*, Si-H bonds and Si-Si bonds in either monohydride sites or dihydride sites are stable to hot spot excitations.

The overall result is that the *MH1* with monohydride bonding species only is stable to bond-breaking excitations with energies as high as 7.0 eV. The *MH2* with both dihydride and monohydride bonding species is less stable than the *MH1*, and does have metastable higher energy dangling-bond states induced by hot spot excitations. However, the energy barriers for the annealing of these dangling-bond states are small (0.04 to 0.11 eV) - generally much smaller than that measured for light-induced defects (0.9 to 1.3 eV) [7]. Hence, these higher-energy configurations may be transient rather than metastable under the experimental conditions.

Experimentally, it is observed that a-Si:H with more dihydride bonding species is more unstable to light-induced degradation [78]. Our results with the *MH2* may qualitatively support this trend, but further work is clearly necessary to clarify a correlation, if any, between dihydride concentration and light-induced defect density.

New Interpretation of the Staebler-Wronski Effect

In this section, we propose a two-level defect system consisting of a bridge-bonded H interstitial and a Si dangling-bond defect that can account for many of the experimental observations of the Staebler-Wronski effect. The calculations in this section are based on molecular dynamics simulations with interatomic potentials

described in Chapter 3. All the potential models used in this section are the same as those in Chapter 3 except the three-body potential for Si-H interactions. The three-body parameters used in this section were modified to achieve a reasonable description of the energies of SiH_4 and both the amorphous and crystal phases [79]. This classical model describes well the collinear Si-H-Si bond-centered (BC) H interstitial in c-Si with an Si-H bond-length of 1.71 Å and cohesive energy of 0.88 eV, in good agreement with values from ab-initio calculations of 1.63 Å and about 1.0 eV, respectively [80].

Using these potentials, we have considered the a-Si:H model containing 10 at.% of H proposed by Guttman and Fong [69] with 54 Si atoms and 6 H atoms in monohydride bonding configurations, and periodic boundary conditions. The a-Si:H model was relaxed to a new minimum of the potential energy with the above potentials at different densities. The lowest energy configuration occurred at a mass density of 0.92 of c-Si, with rms bond-angle deviations of 10.5° and rms bond-length deviations of 0.10 Å for Si-Si and 0.01 Å for Si-H bonds. In the fully relaxed configuration, all the H atoms were incorporated in monohydride bonding configurations, with no coordination defects, a feature qualitatively similar to device-quality a-Si:H. H relaxes the strains and eliminates the large density of coordination defects present in a-Si models without H. We found that this a-Si:H model was very stable to thermal annealing up to 700 K, and no lower energy configuration could be produced by quenching or cooling from elevated temperatures. Hence this a-Si:H model, devoid of unnecessary defects, was a good starting point for the further investigations of the Staebler-Wronski effect.

Experimentally, the light-soaked defect densities reach a saturation value of the

order of 10^{17} cm^{-3} [71, 72], so that the Staebler-Wronski defect occurs with a probability of about 10^{-4} to 10^{-5} per atom. Hence in computer-generated models of up to a few hundred atoms, the Staebler-Wronski defect is not expected to be present. However, it is still possible to "introduce" relevant defects into our finite size models that are connected to light-induced degradation.

Our crucial observation is that a very novel defect can be created in this otherwise stable a-Si:H network by introducing an additional H atom. We find that the extra H atom energetically prefers occupying a bridge-bonded (BB) configuration in which it is bonded to two Si atoms with bond-lengths of 1.71 Å, and a Si-H-Si bond-angle between 140° and 150° [Figure 4.8(a)]. The extra H induces large outward displacements of the two Si neighbors. This result is analogous to well-established first-principles theoretical results that H in c-Si has the lowest energy when occupying a collinear Si-H-Si bond-centered configuration for positive and neutral charge states [80]. Other authors [13, 14, 15, 81] have suggested the collinear bond-centered H interstitial in a-Si:H, but in contrast to these studies, we find that the H interstitial in a-Si:H remains off-center in a bridged configuration.

The longer Si-H bond-length in both BC H in c-Si and the BB H in a-Si:H reflects the weaker Si-H bonding compared to Si-H bonds in silane, or monohydride bonding groups in a-Si:H (where Si-H is 1.50 Å). We calculate a distribution of energies (Figure 4.9) to create a BB H interstitial that lies at least 0.3 eV above the Si-H bond energy (−3.05 eV).

Our key observation is that the H atom can be displaced toward one or the other Si atom resulting in a strong Si-H bond (1.50 to 1.53 Å) with one Si atom and a single dangling bond on the other Si atom [Figure 4.8(b)]. To accommodate the

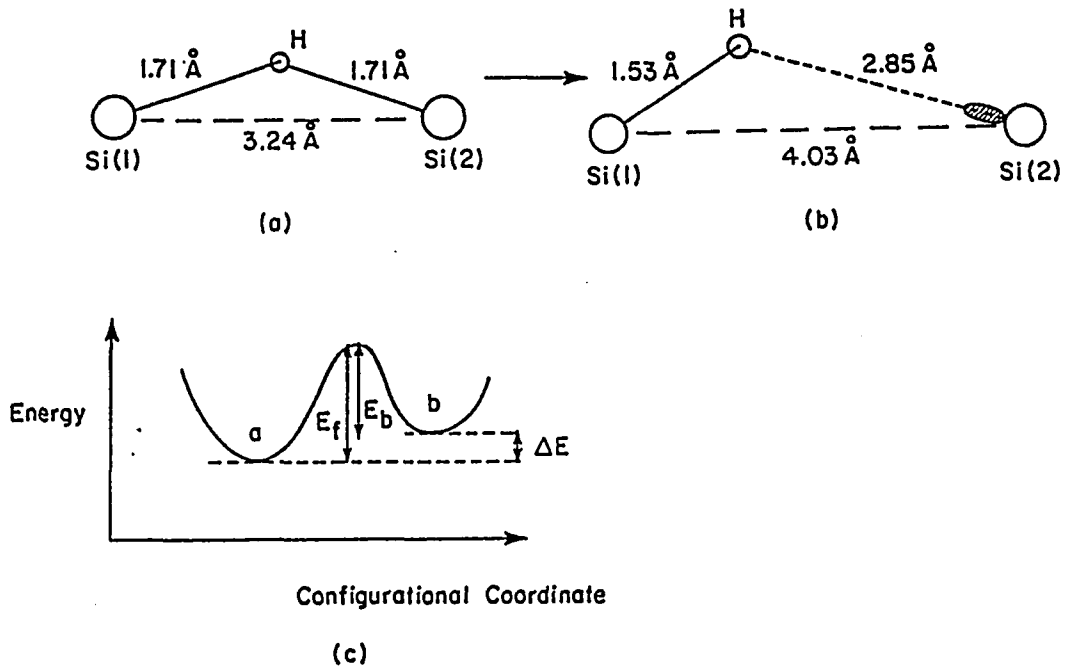

Figure 4.8: (a) Schematic diagram of the bridge-bonded (BB) hydrogen configuration and (b) the resulting metastable configuration with a single dangling bond on one Si-atom. (c) Schematic energy-level diagram connecting these two configurations

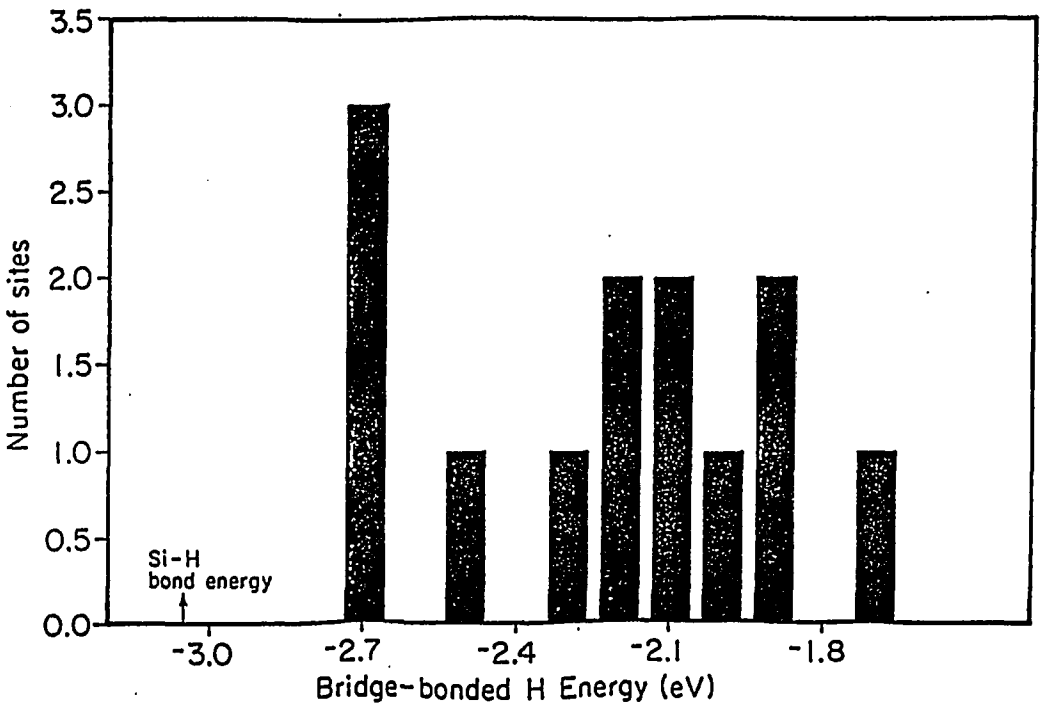

Figure 4.9: Distribution of energies to create a bridge-bonded H interstitial at various sites in the a-Si:H network. For comparison the energy to put the H in a normal Si-H bond (as in a monohydride) is −3.05 eV

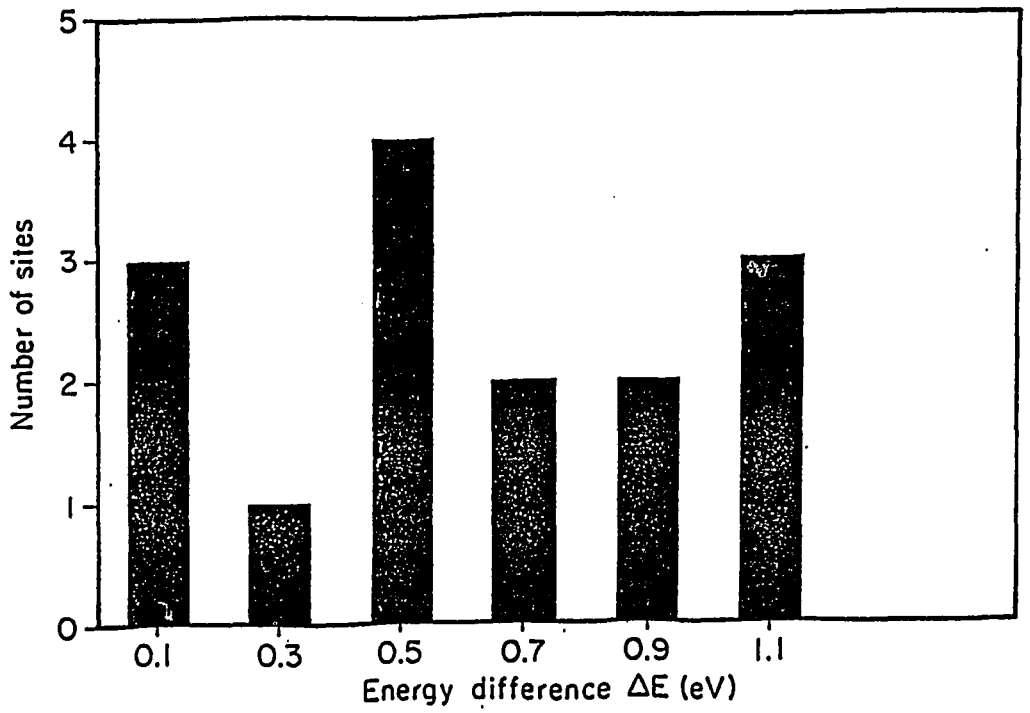

Figure 4.10: Distribution of the energy differences between the metastable dangling bond state and the bridge-bonded H configuration

Si dangling bond, the two Si atoms are pushed outward even further, i.e., relaxation of the amorphous network is essential. The dangling-bond state is a locally stable configuration that has higher energy than the BB state [Figure 4.8(c)], with energy differences ΔE varying from 0.04 eV to 1.2 eV, depending on the particular BB H site examined (Figure 4.10). We note that Street [15] has also suggested the existence of the bond-centered H interstitials in a-Si:H and the dangling-bond state and their relation to both light-induced degradation and H diffusion. Also a diatomic H complex, containing a bond-centered H interstitial, has been proposed by Jackson and coworkers [13, 14], as an alternative model for the Staebler-Wronski effect.

Since the dangling-bond state is locally stable to structural perturbations, we hypothesize that the BB H state is the annealed state of the Staebler-Wronski defect, whereas the dangling-bond state is the metastable defect state, with these two configurations connected by a two-state energy configuration [Figure 4.8(c)]. The height of the energy barrier between these two configurations depends on the ability of the amorphous network to relax during the motion of the H between the two configurations. When the H atom and its two neighboring Si atoms move uniformly between their positions in the BB H state to the dangling-bond state, we estimate an annealing energy barrier E_b of 1.0 - 2.0 eV, whereas this annealing barrier is reduced to 0.2 - 0.3 eV when the entire network is allowed to relax. The complete network relaxation may not be possible on the timescales of the H motion, in which case energy barriers of 1.0 - 2.0 eV are consistent with barriers of 0.9 eV - 1.3 eV obtained from measurements of the annealing of the metastable dangling bond density [7].

We note that the energy barrier to defect formation is higher than that for annealing by the energy difference between dangling-bond and BB H state. In general,

there is a distribution of barrier heights [E_b and E_f, Figure 4.8(c)], and this implies that the kinetics of formation of the metastable defects should follow a stretched exponential behaviour, in agreement with theoretical fits of the experimental saturation behaviour of light-induced defects [82].

We hypothesize that a small density N_{BB} of the BB H configurations are frozen in during the growth process. Then, an a-Si:H sample would have a finite number of such weakly bonded BB H defect centers that could be converted to metastable dangling bond sites during illumination. The saturation of the metastable-defect density is achieved, when the rates of transition from a to b and from b to a [Figure 4.8(c)] are the same. The kinetics of conversion between the two species in the two-level potential diagram can be described by stretched exponential kinetics [82]. During an equilibrium growth process, a density N_{BB} of the weakly bonded species may be produced that is given by

$$N_{BB} = N_H \exp(-\frac{\delta E}{k_B T_s}), \tag{4.7}$$

where T_s is the substrate temperature, and N_H is the total H density of the sample. The thermally activated expression Eq. (4.7) is best approached at low substrate temperatures (about 200° C or below). If we use typical glow-discharge a-Si:H conditions [83] at 200° C where H concentration is 16.5 at.% or N_H is 8.25×10^{21} cm^{-3}, we estimate a density of BB H to be 4.5×10^{17} cm^{-3} using an average δE of 0.4 eV for the energy difference between the Si-H bond energy (−3.05 eV) and the lower energy group of BB H defects from Figure 4.9. We note that even if higher-energy BB H configurations are initially formed, the H could switch to adjacent sites in the lower-energy tail of the distribution in Figure 4.9, so that a lower value of about 0.4 eV for δE is relevant. This estimate of the density of BB H defects is consistent

with measured values of the saturation density of the metastable defects [71, 72]. This picture leads naturally to a finite saturation density and a limited number of metastable-defect sites that can be produced during illumination.

During the creation of the metastable dangling-bond state, the charge state of the defect can change. Our tight-binding electronic structure calculations indicate that the BB H has a defect level in the upper half of the band gap, similar to the result found for bond-centered H in c-Si [80]. If the Fermi level is near mid-gap (i.e., compensated material), the BB H is unfilled and exists in the positive-charge state. The dangling bond is, however, stable in the neutral charge state. Conversion of the BB H to a dangling bond then involves a change in the charge state of the defect with the capture of an electron and a consequent decrease in the conductivity. Details of the microscopic conversion between these two species will require further studies.

A definite prediction of this model is that the metastable dangling-bond defects should have a H atom in their vicinity. In principle, a hyperfine interaction should exist between the H nuclear moment and the dangling-bond spin. However, we expect a distribution of distances between H and the Si dangling bond arising from the amorphous environment, and this may lead to a broadening of ESR line itself rather than a sharp hyperfine feature. The present model leads to a single dangling bond in the light-soaked state in contrast to two dangling bonds in the weak Si bond-breaking model of Stutzmann et al. [7]. H plays a crucial role in the present model, in contrast to the model of Adler [11] where existing charged dangling bonds trap carriers. The saturation of the light-induced defect density arises from a finite number of H induced defect sites in the present model.

CHAPTER 5. CONCLUSIONS

Amorphous silicon and hydrogenated amorphous silicon have been studied with molecular dynamics simulations. The structural, vibrational, and electronic properties of these materials have been studied with computer-generated structural models. The stabilities of a-Si and a-Si:H also have been studied with the aim of understanding microscopic mechanisms underlying light-induced degradation in a-Si:H (the Staebler-Wronski effect [5]).

The amorphous silicon films have been generated with molecular dynamics simulations by simulating Si-cluster deposition processes on a Si(111) substrate. The Biswas-Hamann classical interatomic Si potential [30] has been employed in the calculations. The a-Si films have a lower density of 0.73 - 0.84 than of the crystal, and voids that lead to intense small wave-vector scattering in the static structure factor. A remarkable result is that no floating bonds are found in the a-Si films. Instead, all coordination defects comprise of dangling bonds. This directly contrasts with melt-quenched bulk a-Si models [22], developed with the same potential, that have both dangling and floating bonds. Our interpretation is based on the floating bonds being a very mobile species that can easily diffuse with a bond-switching mechanism [4]. Hence, the floating bonds easily diffuse to either the internal void surfaces or external growing surface, where they recombine with the large number of dangling

bonds present at these surfaces. Both the lack of floating bonds and the presence of voids lead to lower-bond-angle strains in the amorphous films than in the bulk a-Si models. This result is also supported by the study of void structures in bulk a-Si models. Voids of various sizes have been introduced into melt-quenched a-Si models. The voids cause only small changes in the vibrational densities of states.

A new two- and three-body interatomic potential for Si-H interactions has been developed by fitting to ab-initio calculations of the energy of H on a Si cluster and H bond-bending frequencies in a-Si:H. The structural properties of a-Si:H networks developed by this potential together with the Biswas-Hamann Si interatomic potential [30] compared well with experimental measurements. The presence of H atoms reduces strain and disorder relative to networks without H.

We have studied the stability of a-Si models, with no H atoms, against local excitation processes and thermal annealing as a first step toward understanding the Staebler-Wronski effect. A local hot spot has been used to model the non-radiative energy transfer of photo-excited carriers to the system, and structural changes induced by this excitation are studied in detail. Local excitations of the four-coordinated WWW [20] model indicate structural changes that require energy thresholds of 0.8 - 1.0 eV, and primarily occur on weak Si-Si bonds or weakly bonded Si atoms. We have observed the generation of a metastable pair of ESR-active dangling bond defects, induced by local excitations on such a weak bond. In contrast, c-Si is stable to local excitations as large as 8.0 eV.

To investigate bond-breaking models of the Staebler-Wronski effect, we have examined structural changes against local excitations in two a-Si:H models - (1) a 60-atom model with 10 at.% H and only monohydride bonding species and (2)

a 68-atom model with 20.6 at.% H and both monohydride and dihydride bonding species. The important result is that the single phase monohydride-containing a-Si:H model, with no coordination defects or H-induced defects, is stable to bond-breaking excitations. The monohydride-containing a-Si:H model has a H content similar to device-quality materials. This result does not support the suggestion of Stutzmann, Jackson, and Tsai [7] involving rupturing of a weak Si-Si back bond at a monohydride site. Alternatively, the proposed motion of H into the Si-Si bond site may be a very low probability event.

The a-Si:H model with both dihydride and monohydride bonding species is somewhat less stable than the model with only monohydride bonding species. The dihydride-containing a-Si:H model does have higher energy dangling-bond states induced by hot spot excitations, but these can easily anneal back to the initial configuration with annealing barriers of 0.04 - 0.11 eV. These dangling-bond states, that are produced by local excitations, are then not similar to metastable light-induced defect states.

We propose a two-level defect system as a mechanism for the Staebler-Wronski effect in a-Si:H. A bridge-bonded H interstitial defect is identified as the annealed state that can form a higher-energy metastable Si dangling-bond state in the light-soaked state. This two-level defect system can account for various features of light-induced degradation in a-Si:H including the saturation of defect density and metastability of defects. The presence of hydrogen and local H motion play a crucial role in both the metastable defect formation and the annealing of these defects.

Although the time scales of the molecular dynamics simulations performed in this dissertation are several orders less than experimental time scales and the size of

the system studied are finite, we have shown that the theoretical simulations account well for various experimental observations of amorphous silicon and hydrogenated amorphous silicon.

BIBLIOGRAPHY

[1] S. R. Elliott, *Physics of Amorphous Materials* (2nd edition) (Longman Scientific & Technical, England, 1990).

[2] M. H. Brodsky, *Amorphous Semiconductors* (2nd edition) (*Topics in Applied Physics*, vol. 36) (Springer-Verlag, 1985).

[3] L. C. Chen and F. Spaepen, Nature **336**, 366 (1988).

[4] S. T. Pantelides, Phys. Rev. Lett. **57**, 2979 (1986); **58**, 1344 (1987).

[5] D. L. Staebler and C. R. Wronski, Appl. Phys. Lett. **31**, 292 (1977).

[6] C. R. Wronski, *Instabilities in a-Si:H Solar Cells: Materials and Device Issues* (Proc. 21st IEEE PV Specialists Conference, 1990), p. 1487.

[7] M. Stutzmann, W. Jackson, and C. C. Tsai, Phys. Rev. B **32**, 23 (1985).

[8] R. S. Crandall, Phys. Rev. B **43**, 4057 (1991), and references therein.

[9] R. Jones, and G. M. S. Lister, Phil. Mag. B **61**, 881 (1990).

[10] M. Fathallah, Phil. Mag. B **61**, 403 (1990).

[11] D. Adler, J. Phys. (Paris) Colloq. **42**, C4-3 (1981).

[12] S. T. Pantelides, Phys. Rev. B **36**, 3479 (1987).

[13] S. B. Zhang, W. B. Jackson, and D. J. Chadi, Phys. Rev. Lett. **65**, 2575 (1990).

[14] W. Jackson, Phys. Rev. B **41**, 10257 (1990).

[15] R. A. Street, Solar Cells and Proc. Solar Energy Research Institute a-Si:H Program Review, to be published.

[16] D. Redfield and R. H. Bube, Phys. Rev. Lett. **65**, 464 (1990).

[17] R. J. Bell and P. Dean, Nature **212**, 1354 (1966).

[18] S. J. Williams and S. R. Elliott, Proc. Roy. Soc. A **380**, 427 (1982)

[19] J. L. Finney, Proc. Roy. Soc. A **319**, 479 (1970).

[20] F. Wooten, K. Winer, and D. Weaire, Phys. Rev. Lett. **54**, 1392 (1985); K. Winer, Phys. Rev. B **35**, 2366 (1987).

[21] M. D. Kluge, J. R. Ray, and A. Rahman, Phys. Rev. B **36**, 4234 (1987).

[22] R. Biswas, G. S. Grest, and C. M. Soukoulis, Phys. Rev. B **36**, 7437 (1987).

[23] W. D. Luedtke and U. Landman, Phys. Rev. B **37**, 4656 (1988); **40**, 1164 (1989).

[24] R. Car and M. Parrinello, Phys. Rev. Lett. **60**, 204 (1988).

[25] T. Takagi, *Ion Implantation and Ion Beam Processing of Materials*, edited by G. K. Hubler, O. W. Holland, C. R. Clayton, and C. W. White (North-Holland, New York, 1984), p. 501, and references therein.

[26] R. Biswas, G. S. Grest, and C. M. Soukoulis, Phys. Rev. B **38**, 8154 (1988).

[27] P. C. Kelires and J. Tersoff, Phys. Rev. Lett. **61**, 562 (1988).

[28] F. H. Stillinger and T. A. Weber, Phys. Rev. B **31**, 5262 (1985).

[29] J. Tersoff, Phys. Rev. B **37**, 6991 (1988).

[30] R. Biswas and D. R. Hamann, Phys. Rev. B **36**, 6434 (1987).

[31] J. C. Phillips, Phys. Rev. Lett. **58**, 2824 (1987); J. C. Phillips, J. C. Bean, B. A. Wilson, and A. Ourmazd, Nature (London) **325**, 121 (1987).

[32] Parameters of the Biswas-Hamann potential are $A_1 = 0.1422922 \times 10^3$ eV, $A_2 = -0.1070338 \times 10^3$ eV, $\lambda_1 = 0.5200836$ Å^{-2}, $\lambda_2 = 0.4206931$ Å^{-2}, B = 0.1302990×10^2 eV, $\alpha = 0.3034373$ Å^{-2}, $r_c = 3.9527357$ Å, and $\mu = 0.3120580$ Å.

[33] C. W. Gear, *Numerical Initial Value Problems in Ordinary Differential Equations* (Prentice Hall, Englewood Cliffs, 1971).

[34] K. H. Müller, J. Appl. Phys. **61**, 2516 (1987).

[35] K. E. Khor and S. Das Sarma, Chem. Phys. Lett. **134**, 43 (1987), and references therein.

[36] M. Schneider, I. K. Schuller, and A. Rahman, Phys. Rev. B **36**, 1340 (1987).

[37] N. Metropolis, A. Rosenbluth, M. Rosenbluth, A. Teller, and E. Teller, J. Chem. Phys. **21**, 1087 (1953).

[38] P. N. Keating, Phys. Rev. **145**, 637 (1966).

[39] T. A. Postol, C. M. Falco, R. T. Kampwirth, I. K. Schuller, and W. B. Yellon, Phys. Rev. Lett. **45**, 648 (1980).

[40] A. Chenevas-Paule, R. Bellissent, M. Roth, and J. I. Pankove, J. Non-Cryst. Solids **77-78**, 373 (1986).

[41] A. J. Craven, A. J. Patterson, A. R. Long, and J. I. B. Wilson, J. Non-Cryst. Solids **77-78**, 217 (1986).

[42] P. D'Antonio and J. H. Konnert, Phys. Rev. Lett. **43**, 1161 (1979).

[43] N. J. Shevchik and W. Paul, J. Non-Cryst. Solids **16**, 55 (1974).

[44] A. Guinier, G. Fournet, C. B. Walker, and K. L. Yudowitch, *Small Angle Scattering of X-rays* (Wiley, New York, 1955).

[45] R. Biswas, A. M. Bouchard, W. A. Kamitakahara, C. M. Soukoulis, and G. S. Grest, Phys. Rev. Lett. **60**, 2280 (1988).

[46] A. M. Bouchard, R. Biswas, W. A. Kamitakahara, C. M. Soukoulis, and G. S. Grest, Phys. Rev. B **38**, 10499 (1988).

[47] W. A. Kamitakahara, C. M. Soukoulis, H. R. Shanks, U. Buchenau, and G. S. Grest, Phys. Rev. B **36**, 6539 (1987).

[48] J. E. Yehoda, B. Yang, K. Vedam, and R. Messier, J. Vac. Sci. Technol. A **6**, 1631 (1988), and references therein.

[49] *The Physics of Hydrogenated Amorphous Silicon*, edited by D. Joannopoulos and G. Lucovski (Springer-Verlag, New York, 1894).

[50] J. Shinar, R. Shinar, S. Mitra, M. L. Albers, H. R. Shanks, and T. D. Moustakas, Mat. Res. Soc. Symp. Proc. **95**, 183 (1987).

[51] R. Messier and R. C. Ross, J. Appl. Phys. **53**, 6220 (1982).

[52] J. S. Lannin, in *Disordered Semiconductors*, edited by M. Kastner and G. A. Thomas (Plenum, New York, 1987), p. 283.

[53] L. Guttman, Phys. Rev. B **23**, 1866 (1981).

[54] W. D. Luedtke and U. Landman, Phys. Rev. B **40**, 1164 (1989).

[55] W. E. Spear and P. G. Le Comber, Phil. Mag. **33**, 935, (1976).

[56] T. D. Moustakas, J. Electronic Mat. **8**, 391 (1979).

[57] J. B. Boyce and M. Stutzmann, Phys. Rev. Lett. **54**, 565 (1985).

[58] H. V. Lohneysen, H. J. Schink, and W. Beyer, Phys. Rev. Lett. **52**, 549 (1984).

[59] J. E. Graebner, L. C. Allen, and B. Golding, Phys. Rev. B **31**, 904 (1985).

[60] I. Kwon, R. Biswas, G. S. Grest, and C. M. Soukoulis, Phys. Rev. B **41**, 3678 (1990).

[61] W. A. Kamitakahara, R. Biswas, A. M. Bouchard, F. Gompf, and J. B. Suck, Mat. Res. Soc. Symp. Proc. **166**, 361 (1990).

[62] K. Winer and F. Wooten, Phys. Stat. Sol. (b) **124**, 473 (1984).

[63] Guido L. Chiarotti, F. Buda, R. C. Car, and M. Parrinello, Mat. Res. Soc. Symp. Proc. **163**, 383 (1990).

[64] N. Mousseau and L. J. Lewis, Phys. Rev. B **41**, 3702 (1990); **43**, 9810 (1991).

[65] Parameters of the two-body potential for Si-H interactions are $C_1 = 0.1113967 \times 10^4$ eV, $C_2 = -0.7 \times 10^3$ eV, $\kappa_1 = 2.7801$ Å^{-1}, and $\kappa_2 = 2.3616$ Å^{-1}.

[66] A. Selmani, D. R. Salahub, and A. Yelson, Surface Science **202**, 269 (1988).

[67] Parameters of the three-body potential are $B_H = 0.226526 \times 10^2$ eV, $\alpha_H = 0.60334$ Å^{-2}, $r_{c_2} = 1.8$ Å, and $\mu_2 = 0.2$ Å.

[68] Parameters of the potential for H-H interactions are $\epsilon = 0.147$ eV, $\alpha_{HH} = 15.19$, and $\sigma = 1.9$ Å.

[69] L. Guttman and C. Y. Fong, Phys. Rev. B **26**, 6756 (1982).

[70] R. Bellisent, A. Menelle, W. S. Howells, Adrian C. Wright, T. M. Brunier, R. N. Sinclair, and F. Jansen, Physica B **156** & **157**, 217 (1989).

[71] H. R. Park, J. Z. Liu, and S. Wagner, Appl. Phys. Lett. **55**, 2658 (1989).

[72] H. R. Park, J. Z. Liu, P. Roca i Cabarrocas, A. Maruyama, M. Isomura, S. Wagner, J. R. Abelson, and F. Finger, Mat. Res. Soc. Symp. Proc. **192**, 751 (1990); Appl. Phys. Lett. **57**, 1440 (1990).

[73] Parameters of the Stillinger-Weber potential are A = 7.0495556277, B = 0.6022245584, p = 4, q = 0, a = 1.80, λ = 21.0, γ = 1.20, σ = 0.20951 nm, and $\epsilon = 3.4723 \times 10^{-12}$ erg/at. pair.

[74] P. Masri and A. M. Stoneham, in *Proceedings of the Thirteenth International Conference on Defects in Semiconductors*, edited by L. C. Kimmerling and J. M. Parsey (American Institute of Mechanical Engineers, New York, 1985).

[75] J. D. Weeks, J. C. Tully, and L. C. Kimmerling, Phys. Rev. B **12**, 3286 (1975).

[76] D. J. Chadi, Phys. Rev. Lett. **41**, 1062 (1978); Phys. Rev. B **19**, 2074 (1979); Phys. Rev. B **29**, 785 (1984); Phys. Rev. Lett. **59**, 1961 (1988).

[77] B. Min; Y. H. Lee, C. Z. Wang, K. M. Ho, and C. T. Chan, to be published.

[78] V. L. Dalal and C. Fuleiman, Mat. Res. Soc. Sym. Proc. **149**, 601 (1989).

[79] Parameters are $B_H = 0.576828 \times 10$ eV and $\alpha_H = 0.08027$ Å^{-2}. These parameters give better description for H interstitial energies, but less satisfactory for vibrational properties of H in a-Si:H.

[80] C. G. Van de Walle, P. J. H. Denteneer, and S. T. Pantelides, Phys. Rev. B. **39**, 10791 (1989).

[81] R. Fisch and D. C. Licciardello, Phys. Rev. Lett. **41**, 889 (1978).

[82] D. Redfield and R. H. Bube, Appl. Phys. Lett. **54**, 1037 (1989).

[83] See for example H. Matsunami, T. Shirafuji, T. Fuyuki, and M. Yoshimoto, Mat. Res. Soc. Symp. Proc. **192**, 505 (1990).